Dual-Polarization Radar Characteristics of Tropical Cyclone Tornadic and Nontornadic Supercells

MICHAELA J. WOOD[a] AND MATTHEW S. VAN DEN BROEKE[a]

[a] *Department of Earth and Atmospheric Sciences, University of Nebraska–Lincoln, Lincoln, Nebraska*

(Manuscript received 8 May 2024, in final form 27 November 2024, accepted 17 December 2024)

ABSTRACT: Landfalling tropical cyclones (TCs) contain highly sheared environments that are conducive for supercell thunderstorm development. These TC supercells can produce tornadoes, often with little warning. In this study, dual-polarization radar signatures of tornadic and nontornadic TC supercells are examined in the context of known extratropical supercell radar signatures. Prior studies have only presented dual-polarization characteristics of TC supercells using a case study approach. Therefore, this paper aims to create a more comprehensive picture with a larger sample of cases, and an attempt is made to distinguish differences between tornadic and nontornadic TC supercells that may hold operational promise. The environments and characteristic structures of these supercells are notably different from prior conceptual models of supercells developed. Differential reflectivity Z_{DR} columns are shallower in TC supercells when compared to their extratropical counterparts. The Z_{DR} columns are also less common in TC cases. The Z_{DR} arc is more pronounced in TC supercells, with maximum and mean Z_{DR} values within the arcs being larger. Separation angle between the specific differential phase K_{DP} foot and Z_{DR} arc is larger in TC supercells than in extratropical supercells. Tornadic TC supercells had significantly stronger low-level mesocyclones than nontornadic TC supercells as measured by normalized rotation (NROT). The observed differences may help operational meteorologists use these signatures more effectively in warning decisions and motive further research into the evolution of dual-polarization signatures in tornadic and nontornadic TC supercells.

SIGNIFICANCE STATEMENT: Supercell thunderstorms are supported in the highly sheared environments of tropical cyclones. Recurring dual-polarization radar signatures can provide insight into the vertical motion and size-sorting processes occurring in supercells which might be beneficial for operational meteorologists. In this study, dual-polarization signatures are compared between tornadic and nontornadic tropical cyclone supercells and examined against their extratropical counterparts. Various differences were discovered between these signatures in tropical cyclone versus extratropical supercells, which could be attributed to differences in their thermodynamic and kinematic environments. Statistically significant differences were not found between dual-polarization signatures in tornadic and nontornadic tropical cyclone supercells.

KEYWORDS: Supercells; Tropical cyclones; Radars/Radar observations

1. Introduction

Tropical cyclone (TC) rainbands often contain embedded supercells. These TC supercells have been thoroughly described in previous literature and have some features that contrast with typical extratropical supercells (McCaul 1991; Spratt et al. 1997). TC supercells may show similarities to extratropical "miniature" supercells as they are smaller in horizontal and vertical extent (Davies 1990; Knupp et al. 1998; Edwards 2012). The small size of TC supercells makes them difficult to sample with Weather Surveillance Radar-1988 Doppler (WSR-88D) resolutions (Spratt and Nash 1995)—their features appear much subtler compared to extratropical supercells, especially at greater range as the beam broadens (e.g., Devanas et al. 2008) but are typically still identifiable. TC supercells may have relatively weak updraft rotation, and their lifespan can range from minutes to several hours (McCaul et al. 2004; Edwards 2012). Poor radar resolution makes it difficult to distinguish tornadic vortex (or debris) signatures in small-sized TC supercells at greater distances from a WSR-88D. The limitations of radar resolution can make issuing severe thunderstorm and tornado warnings more challenging compared to traditional extratropical supercells.

TC supercell environments typically differ from those commonly present in extratropical environments and are characterized by increased lower-tropospheric vertical wind shear and limited buoyancy (McCaul 1991). Buoyancy in TC supercell environments is substantially reduced [convective available potential energy (CAPE) < 1000 J kg^{-1}] with accumulated CAPE values maximized in the lowest 3–4 km, whereas Great Plains supercell environments are maximized closer to 10-km altitude (McCaul 1991). A similar case is seen with vertical wind shear as low-level wind shear is increased (0–1-km shear approximately 15.4 m s^{-1}) and maximized near 2–3-km altitude in TC supercell environments, whereas Great Plains supercell environments peak above 10 km (McCaul 1991). Supercells are favored in the right-front sector (with respect to TC motion) of the Northern Hemisphere TCs where storm-relative helicity (SRH) is maximized downshear from the TC center in a region collocated with maximum instability (Molinari and Vollaro 2010). Supercells are most common in the outer region of a TC (>200 km from the center) within 48 h of landfall (McCaul 1991; Schultz and Cecil 2009; Molinari and Vollaro 2008) and

Corresponding author: Matthew S. Van Den Broeke, mvandenbroeke2@unl.edu

DOI: 10.1175/MWR-D-24-0080.1

may also spawn tornadoes. Tornadoes associated with these supercells are typically weak—of more than 1800 TC tornadoes from 1950 to 2007, 81.1% were F0 or F1 (Schultz and Cecil 2009). Even though TC tornadoes result in a small fraction of TC damages, issuing appropriate warnings remains an important challenge. Tornadic and nontornadic TC supercells often occur in proximity, ruling out the use of large environmental differences to aid in the warning decision-making process (Spratt et al. 1997) and highlighting the value of radar observations (Healey and Van Den Broeke 2023).

The operational Next Generation Weather Radar (NEXRAD) network in the United States was upgraded to include dual-polarization capabilities between 2011 and 2013, which provide additional information about hydrometeor classification and microphysical processes occurring in convective storms (e.g., Scharfenberg et al. 2005). Additional radar products are generated since this upgrade includes correlation coefficient ρ_{hv}, differential reflectivity Z_{DR}, and specific differential phase K_{DP}. The ρ_{hv} measures the diversity of scatterers in a sample volume by quantifying the correlation between the received horizontally and vertically polarized signals. Values of ρ_{hv} near 1 indicate scatterers with a consistent shape and orientation, such as uniform raindrops, while values decreasing from 1 indicate increasing variability. The Z_{DR} is the difference between the horizontally and vertically polarized reflectivity value and can give insight into the mean shape of scatterers in a sample volume (Seliga and Bringi 1976). Positive Z_{DR} is associated with scatterers whose major axes are oriented horizontally. Raindrops become more oblate as they grow (Pruppacher and Pitter 1971), giving larger raindrops higher positive Z_{DR} values. The K_{DP} is a measure of the phase shift per unit distance between the horizontally and vertically polarized pulses and can give insight into the concentration of droplets in a sample volume. For more details of these variables, see Kumjian (2013).

Several recurring dual-polarization signatures may contain beneficial information about a supercell's tornadic potential. A Z_{DR} column is a region of enhanced positive Z_{DR} values above the environmental 0°C level collocated (or almost so) with a convective updraft (Herzegh and Jameson 1992; Kumjian and Ryzhkov 2008; Kumjian et al. 2014; Wienhoff et al. 2018). The Z_{DR} columns are relatively narrow (4–8 km wide) and can be more than 3 km deep (Kumjian and Ryzhkov 2008; Kumjian et al. 2014). Environmental thermodynamic characteristics including the lifting condensation level (LCL) height may play a role in updraft depth and width (Mulholland et al. 2021). Van Den Broeke (2016) also found that the LCL height and CAPE may play a role in Z_{DR} column size and depth. This Z_{DR} enhancement is due to oblate liquid drops and water-coated hailstones lofted above the 0°C level by the updraft. The Z_{DR} column can be used to infer updraft area and depth (Kumjian et al. 2010, 2014). Observational and modeling studies suggest that changes in the Z_{DR} column area and depth can provide insights into updraft strength (Kumjian et al. 2010; Van Den Broeke 2016), with the areal extent potentially helping to infer a supercell's tornadic potential (French and Kingfield 2021) and peak tornado intensity (Trapp et al. 2017, 2018; Marion et al. 2019; Sessa and Trapp 2020). In prior modeling studies, it was found that environments with higher LCLs produced wider, deeper, and stronger updrafts than those with lower LCLs (Mulholland et al. 2021). Environmental kinematic factors including storm-relative flow and deep-layer shear may also provide insight into updraft size and, therefore, Z_{DR} column characteristics (Warren et al. 2017; Peters et al. 2019, 2020). Previous small-sample studies show potential for Z_{DR} columns to help distinguish tornadic and nontornadic supercells—tornadic extratropical supercells tend to have wider Z_{DR} columns than nontornadic extratropical supercells (Van Den Broeke 2017, 2020; French and Kingfield 2021).

The Z_{DR} arcs are elongated regions of enhanced Z_{DR} values along a supercell's forward flank (Kumjian and Ryzhkov 2008; Dawson et al. 2014). This low-level signature is typically 1–2 km in depth with values over 2 dB but may exceed 4–5 dB (Kumjian and Ryzhkov 2008, 2009). Wind vectors typically increase in magnitude and veer with height in right-moving supercell environments, allowing a size-sorting process that advects smaller drops farther into the interior of the forward-flank precipitation region, while larger drops fall closer to the right edge of the forward flank (Kumjian and Ryzhkov 2007). The mean storm-relative wind in the sorting layer is an important variable relating to this size-sorting process (Dawson et al. 2015). In some cases, the life cycle of a supercell's mesocyclone has been linked to the structure and intensity of the Z_{DR} arc (Kumjian et al. 2010; Palmer et al. 2011). In a small set of cases, Z_{DR} arc orientation and maximum value within the arc may help differentiate tornadic and nontornadic supercells—tornadic supercells tend to have increased arc curvature and maximum Z_{DR} values within the arc (Ryzhkov et al. 2005; Palmer et al. 2011; Crowe et al. 2012). Previous work using a small extratropical supercell sample found larger mean Z_{DR} arc values and a larger areal extent of the 3.5-dB Z_{DR} arc in tornadic supercells than in nontornadic supercells (Van Den Broeke 2017, 2021).

Finally, the K_{DP} foot is a region of enhanced K_{DP} values in the low levels of a supercell's forward flank (Romine et al. 2008). The separation angle and horizontal separation distance between the storm motion vector and a vector between the Z_{DR} arc and K_{DP} maximum centroids give insight into active size-sorting processes and mesocyclone strength (Kumjian and Ryzhkov 2009; Dawson et al. 2014). This separation occurs as storm-relative winds carry smaller drops farther than larger drops, due to the increased terminal velocity of larger raindrops (Kumjian and Ryzhkov 2012; Dawson et al. 2015). Both the separation distance and separation angle of these features are correlated with the mean storm-relative wind and SRH in the sorting layer (Loeffler and Kumjian 2020; Loeffler et al. 2023). Connections have also been made between the separation of these features and the low-level wind shear within a supercell (Crowe et al. 2012). It has been shown that increased values of SRH are correlated with increased separation distance and increasingly orthogonal separation angles when compared to the shear vector of the layer (Loeffler and Kumjian 2020).

Separation between the Z_{DR} arc and K_{DP} foot may give insight into the tornadic potential of a supercell (Crowe et al. 2012; Loeffler et al. 2020, 2023). Contrasting results have been found in regard to effects of separation distance and tornadic potential between modeling and observational work (Crowe et al. 2012;

Martinaitis 2017; Loeffler et al. 2020, 2023). However, prior work using both observations and modeling has found separation vectors more orthogonal to the storm motion in tornadic cases, while nontornadic cases exhibited a more parallel separation angle (Crowe et al. 2009; Loeffler et al. 2020; Van Den Broeke 2008; Loeffler et al. 2023). Loeffler et al. (2020) used observations to investigate this difference, associating the K_{DP} foot with enhanced precipitation and negative buoyancy (Carlin and Ryzhkov 2019). The study concluded that the parallel separation angle places this area of negative buoyancy in an unfavorably close area to the updraft, while a perpendicular angle is farther removed and, therefore, in a more favorable location for tornadogenesis (Markowski et al. 2002; Markowski and Richardson 2017). Similar results were also produced in Loeffler et al. (2023), where modeling work was used to visualize an unfavorable parallel separation angle of the K_{DP} foot. This orientation resulted from enhanced rearward storm-relative flow in the size-sorting layer, thereby reducing the baroclinic production of circulation in nontornadic simulations compared to tornadic simulations. Similar observational results were seen in tropical cyclone supercells using a small sample size (Crowe et al. 2009; Martinaitis 2017).

Relatively little work has described the dual-polarization characteristics of TC supercells, with most studies using a case study approach. A more detailed examination is needed to determine if it will be possible to improve tornado warning skill and decrease the relatively high false alarm ratio (FAR) for these supercells (NWS 2012) using dual-polarization characteristics. Previous work indicates that polarimetric characteristics may help distinguish between tornadic and nontornadic extratropical supercells. The goal of this study is to test several hypotheses in order to establish similarities and differences between the dual-polarization characteristics of TC and extratropical supercells and focus on potential use of the dual-polarization signatures to distinguish tornadic from nontornadic TC supercells. The hypotheses are listed below:

1) The Z_{DR} columns will be narrower and shallower in TC supercells than extratropical supercells due to a combination of their higher environmental freezing levels (McCaul 1991; Davies 2006), lower LCLs (Davies 2006; Mulholland et al. 2021), weaker deep-layer shear (McCaul 1991; Davies 2006; Warren et al. 2017; Peters et al. 2019, 2020), and shallower updrafts (Spratt et al. 1997; Schneider and Sharp 2007; Edwards 2012).
2) Analogous with prior findings for extratropical supercells (e.g., Van Den Broeke 2017, 2020; French and Kingfield 2021; Healey and Van Den Broeke 2023), we hypothesize that tornadic TC supercells will have larger Z_{DR} columns than nontornadic TC supercells.
3) The increased low-level wind shear in TC environments compared to extratropical supercell environments leads to the hypothesis that Z_{DR} arcs will often be present across multiple radar volume scans and with a greater maximum Z_{DR} value within the arc in TC supercells (McCaul 1991; Nowotarski et al. 2021).
4) Due to the increased low-level wind shear and enhanced low-level SRH in TC environments (McCaul 1991; Davies 2006), it is hypothesized that there will be an increase in the separation angle and separation distance when normalized by storm size between the K_{DP} foot and the Z_{DR} arc in TC supercells when compared to extratropical supercells.
5) Previous work investigating Z_{DR} arc and K_{DP} foot separation in extratropical supercells, alongside similar results with TC supercells, suggests the hypothesis that tornadic TC supercells will exhibit a greater (more orthogonal) separation angle and distance between the Z_{DR} arc and the K_{DP} foot compared to nontornadic cases.

Establishing differences that may support or refute the aforementioned hypotheses can be beneficial for operational meteorologists in order to better understand storm-scale features and help identify which supercells are more likely to produce tornadoes in TC environments.

2. Data and methods

a. *Tropical cyclone supercell identification and classification*

To create a large dataset of supercells associated with TCs, a manual analysis was performed to find times with convection or widespread reflectivity ≥ 35 dBZ with at least occasional discrete elements (e.g., individual storm cells with reflectivity ≥ 40 dBZ rather than just widespread uniform stratiform precipitation). These events were required to be within 100 km of a dual-polarization WSR-88D and associated with a TC. This manual analysis was conducted between the 2011 and 2021 TC seasons. Convection was required to be 300 km inland of the coast and during the 48 h following landfall to be included in this study. We identified 57 time periods that satisfied our criteria (Table 1).

A modified version of the National Severe Storms Laboratory (NSSL) mesocyclone detection algorithm (MDA; Stumpf et al. 1998) was used to identify supercells within these time periods. The algorithm requires input of a specific radar location and time to gather four-dimensional radial velocity data. Preprocessing of the data includes the use of the WSR-88D system velocity dealiasing scheme (Eilts and Smith 1990) with adaptable parameter modifications to improve its function (Conway et al. 1995). The algorithm begins at the one-dimensional level in which cyclonic azimuthal shear segments are identified. These shear segments form horizontal associations for two-dimensional features followed by vertical associations for three-dimensional features. The fourth-dimensional level is then completed as features are tracked in time (Stumpf et al. 1998). The MDA includes tunable parameters to adjust the sensitivity of mesocyclone detections while removing false detections from nonmeteorological scatterers such as ground clutter.

The modified NSSL MDA was applied to each time period identified during the manual analysis to consistently detect TC supercells. The MDA detections were cross examined with radar data. Time series of longitude and latitude produced by the MDA for each detection were plotted to ensure that detections contain characteristic radar signatures of supercells as described by Thompson et al. (2003). All false detections were

TABLE 1. Manually identified time periods with TC supercells in close proximity to a WSR-88D radar after the dual-polarization upgrade between the 2011 and 2021 TC season.

Time period	Date(s)	TC	Radar	Analysis period	Supercells identified
1	27 Aug 2011	Irene	KMHX	0000–1000 UTC	19
2	27 May 2012	Beryl	KJAX	1630–2200 UTC	1
3	28 May 2012	Beryl	KCAE	1430–2300 UTC	0
4	23–25 Jun 2012	Debby	KTBW	1900–0300 UTC	15
5	25 Jun 2012	Debby	KJAX	0630–1500 UTC	7
6	6 Jun 2013	Andrea	KAMX	1000–1300 UTC	5
7	6 Jun 2013	Andrea	KTBW	1430–1600 UTC	4
8	6 Jun 2013	Andrea	KJAX	2000–2230 UTC	0
9	7 Jun 2013	Andrea	KLTX	0500–1300 UTC	6
10	7 Jun 2013	Andrea	KMHX	0630–1200 UTC	9
11	3 Jul 2014	Arthur	KCLX	0600–0800 UTC	0
12	3 Jul 2014	Arthur	KLTX	0900–2130 UTC	6
13	3 Jul 2014	Arthur	KMHX	1730–0000 UTC	3
14	4 Jul 2014	Arthur	KAKQ	0400–0900 UTC	3
15	8 May 2015	Ana	KMHX	1500–2200 UTC	1
16	10 May 2015	Ana	KAKQ	1700–2000 UTC	0
17	16 Jun 2015	Bill	KHGX	1130–1930 UTC	2
18	31 May 2016	Bonnie	KLTX	1300–2100 UTC	0
19	31 May–1 Jun 2016	Bonnie	KMHX	1600–1500 UTC	0
20	7 Oct 2016	Matthew	KJAX	0100–1200 UTC	2
21	8 Oct 2016	Matthew	KLTX	1030–1430 UTC	5
22	8 Oct 2016	Matthew	KMHX	1500–2130 UTC	4
23	21 Jun 2017	Cindy	KLIX	0500–1430 UTC	6
24	22 Jun 2017	Cindy	KLCH	0930–1430 UTC	1
25	25 Aug 2017	Harvey	KCRP	0400–0800 UTC	0
26	25–26 Aug 2017	Harvey	KHGX	0800–1200 UTC	14
27	9–10 Sep 2017	Irma	KAMX	1500–1230 UTC	6
28	7 Oct 2017	Nate	KMOB	1800–2330 UTC	7
29	28 May 2018	Alberto	KTLH	0500–2000 UTC	1
30	28 May 2018	Alberto	KMXX	1730–2030 UTC	0
31	10 Oct 2018	Michael	KTLH	0700–1000 UTC	0
32	10 Oct 2018	Michael	KJGX	1730–2130 UTC	2
33	13 Jul 2019	Barry	KSHV	1900–2300 UTC	0
34	5 Sep 2019	Dorian	KLTX	0630–1230 UTC	13
35	5 Sep 2019	Dorian	KMHX	1230–2130 UTC	13
36	17–18 Sep 2019	Imelda	KHGX	2330–0700 UTC	2
37	27 May 2020	Bertha	KMHX	1745–1845 UTC	0
38	7 Jun 2020	Cristobal	KMOB	1030–1400 UTC	9
39	25 Jul 2020	Hanna	KCRP	0700–1400 UTC	3
40	25 Jul 2020	Hanna	KHGX	1500–2300 UTC	3
41	2 Aug 2020	Isaias	KMLB	1100–1700 UTC	0
42	2 Aug 2020	Isaias	KJAX	1500–2200 UTC	0
43	4 Aug 2020	Isaias	KMHX	0000–0630 UTC	8
44	16 Sep 2020	Sally	KEVX	0800–1030 UTC	7
45	21–22 Sep 2020	Beta	KHGX	1430–0700 UTC	0
46	10 Oct 2020	Delta	KGWX	1600–2200 UTC	6
47	28–29 Oct 2020	Zeta	KMOB	2230–0200 UTC	7
48	9 Nov 2020	Eta	KAMX	0530–1100 UTC	3
49	19 Jun 2021	Claudette	KLIX	0500–1500 UTC	0
50	19 Jun 2021	Claudette	KBMX	1420–1600 UTC	0
51	28 Jun 2021	Danny	KCLX	2200–2330 UTC	0
52	7 Jul 2021	Elsa	KTBW	0230–1100 UTC	6
53	7 Jul 2021	Elsa	KJAX	1800–2330 UTC	4
54	16 Aug 2021	Fred	KLTH	1600–1800 UTC	2
55	29–30 Aug 2021	Ida	KLIX	2130–0100 UTC	0
56	8 Sep 2021	Mindy	KLTH	1830–2200 UTC	1
57	13 Sep 2021	Nicholas	KHGX	2200–0000 UTC	0

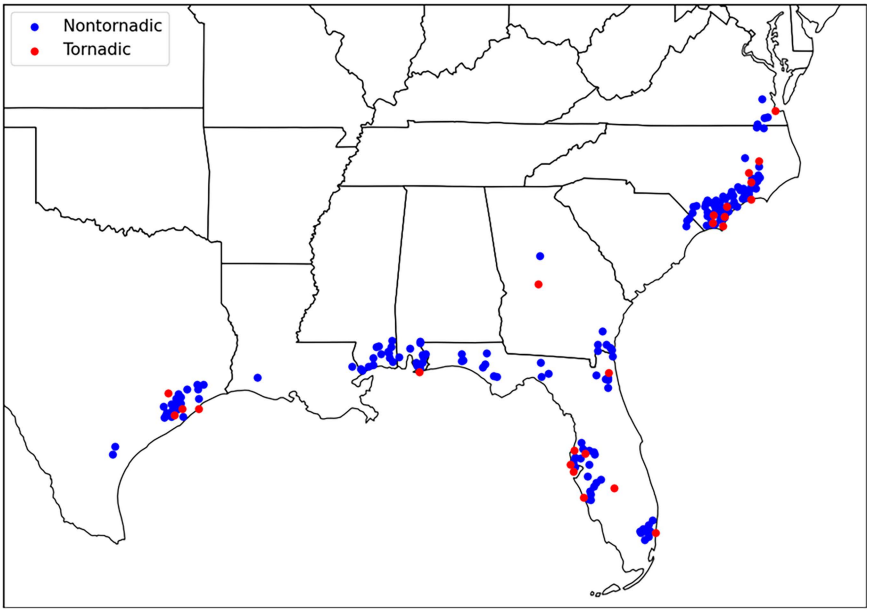

FIG. 1. Geographical location of all 216 TC supercell cases. The blue dots indicate NT cases at the time of maximum NROT, and red dots indicate TOR cases at the time of the first tornado report.

discarded. Detections associated with supercells were required to be within 100 km of a WSR-88D over at least four successive base scans to improve the quantification of low-level dual-polarization signatures (e.g., the Z_{DR} arc). Supercells that met the aforementioned criteria but became undetected at some point in their lifetime only to return as a detectable supercell later are counted as the same supercell. Supercells that underwent mergers or splits during the analysis period were not included. Detected supercells must also be over land since supercells over the ocean may be tornadic with no report. A total of 216 supercells meeting these criteria make up our TC supercell dataset. These supercells had a median lifespan of 57 min with a range between 23 and 181 min within the aforementioned criteria.

Supercells were classified as tornadic or nontornadic based on tornado reports from the NCEI Storm Events Database (https://www.ncdc.noaa.gov/stormevents/). Starting and ending latitude and longitude for tornado reports were plotted to find associated supercells in the TC supercell dataset. We identified 192 nontornadic and 24 tornadic TC supercells (Fig. 1), four of which produced multiple tornadoes (Table 2). The tornado reports included 18 EF0 tornadoes, 12 EF1 tornadoes, and 1 EF2 tornado (Table 2). While the Storm Events Database is the most accurate archive for severe weather reports, it is possible that a "nontornadic" supercell was tornadic but missing an official report. A missing report is possible if the tornado causes little to no damage, occurs in conditions with limited visibility, and/or is embedded in strong straight-line winds (Trapp et al. 2006).

The extratropical dataset, used for comparison with the TC cases, contains 206 supercells from 2012 to 2020. This dataset includes 103 tornadic and 103 nontornadic supercells described by Wilson and Van Den Broeke (2022). Supercells in this dataset include typical supercell reflectivity structures (e.g., hook echoes and bounded weak echo regions), a midlevel mesocyclone maintained for ≥30 min, and at least four successive radar scans with the forward-flank region sampled <1 km above the radar level.

b. *Environmental data*

Environmental data were gathered for each supercell in the TC and extratropical dataset in order to identify environmental differences and compare environmental characteristics to dual-polarization signatures. Proximity soundings from the NCEI archive of Rapid Refresh (RAP; Benjamin et al. 2016) model analysis were obtained for each supercell from the Thematic Real-Time Environmental Distributed Data Services (THREDDS) server. RAP model soundings include 51 vertical levels with a horizontal grid spacing of 13 km. Environments for the 19 cases before 1 May 2012 were from the Rapid Update Cycle (RUC) model which included 40 vertical levels and a horizontal grid spacing of 40 km. For the nontornadic cases, RAP model soundings were obtained at the closest hour to the supercell's maximum low-level rotation and identified using normalized rotation (NROT). NROT is calculated using the range-normalized azimuthal shear value associated with a rotation couplet. These values range from 0 to 5 for cyclonic cases and from 0 to −5 for anticyclonic cases. Values over 1 (<−1 for anticyclonic) indicate substantial cyclonic rotation (Cooper and Vorst 2016). If maximum NROT occurred 25–35 min after the hour, a RAP model sounding was obtained from the bottom and top of surrounding hours and averaged to estimate environmental conditions midway through the hour. A similar procedure was followed to identify RAP

TABLE 2. Information regarding tornado reports in the TC TOR supercell cases. Column one indicates the associated TC, column two lists the date, column three lists the start and end times (UTC) of the tornado, columns four and five list the start longitude and latitude of the tornado report, and column six lists the rating of the tornado.

TC	Date	Time period	Start lon (°)	Start lat (°)	Rating
Debby	24 Jun 2012	1940–1943 UTC	−82.844	27.878	EF1
Debby	24 Jun 2012	1923–1930 UTC	−81.440	27.270	EF1
Debby	24 Jun 2012	2039–2041 UTC	−82.375	28.151	EF0
Debby	24 Jun 2012	2117–2119 UTC	−82.715	28.237	EF1
Debby	24 Jun 2012	0021–0025 UTC	−82.740	27.700	EF1
Andrea	6 Jun 2013	1513–1516 UTC	−82.414	27.027	EF0
Arthur	4 Jul 2014	0540–0541 UTC	−76.270	36.920	EF0
Harvey	25 Aug 2017	1918–1919 UTC	−94.770	29.310	EF0
Harvey	25 Aug 2017	2311–2320 UTC	−95.545	29.146	EF0
Harvey	25 Aug 2017	0528–0537 UTC	−95.305	29.299	EF0
Harvey	25 Aug 2017	0550–0557 UTC	−95.450	29.438	EF0
Harvey	25 Aug 2017	0550–0552 UTC	−95.452	29.438	EF1
Harvey	25 Aug 2017	0552–0553 UTC	−95.460	29.448	EF1
Harvey	25 Aug 2017	0556–0559 UTC	−95.517	29.487	EF1
Harvey	26 Aug 2017	0712–0714 UTC	−96.760	29.700	EF0
Irma	9 Sep 2017	2235–2239 UTC	−80.104	26.138	EF0
Nate	7 Oct 2017	1858–1859 UTC	−87.693	30.246	EF0
Michael	10 Oct 2018	1932–1936 UTC	−83.880	32.460	EF0
Michael	10 Oct 2018	1958–2007 UTC	−84.027	32.653	EF1
Dorian	5 Sep 2019	0923–0926 UTC	−78.265	34.062	EF1
Dorian	5 Sep 2019	0919–0925 UTC	−77.940	33.969	EF0
Dorian	5 Sep 2019	1037–1041 UTC	−78.247	34.252	EF0
Dorian	5 Sep 2019	1017–1022 UTC	−78.265	34.062	EF0
Dorian	5 Sep 2019	1039–1041 UTC	−77.940	33.969	EF0
Dorian	5 Sep 2019	1145–1153 UTC	−78.247	34.352	EF0
Dorian	5 Sep 2019	1302–1331 UTC	−77.900	34.221	EF2
Dorian	5 Sep 2019	1830–1838 UTC	−77.120	35.350	EF0
Dorian	5 Sep 2019	2100–2101 UTC	−77.038	35.106	EF0
Isaias	3 Aug 2020	0448–0449 UTC	−76.801	35.644	EF1
Isaias	3 Aug 2020	0450–0451 UTC	−76.729	35.426	EF1
Elsa	7 Jul 2021	2045–2051 UTC	−81.607	30.281	EF1

model sounding times for tornadic supercells, in which the sounding time was the hour closest to the first tornado report.

The RAP model sounding was required to be ≤40 km from the supercell in the inflow region, determined using radar data from the NEXRAD archive at the time of the RAP model sounding. A marker was placed on the reflectivity gradient near the weak echo region (WER). This tight reflectivity gradient is a proxy for the supercell updraft region and represents a region where air is being ingested into the supercell (Potvin et al. 2010). From this marker, a RAP sounding location was chosen 40 km from the supercell following the inflow wind direction (Fig. 2). Extratropical RAP soundings were obtained by Wilson and Van Den Broeke (2022) following the same methodology, though these may be from up to 80 km away from the supercell if needed to avoid contamination from surrounding convection. Thermodynamic, kinematic, and derived environmental variables were calculated using the Meteorological Python (MetPy version 1.4; May et al. 2017) and Sounding and Hodograph Analysis and Research Program in Python (SHARPpy version 1.4; Blumberg et al. 2017) packages.

Care was taken to ensure that soundings were not contaminated by nearby overlapping updraft regions, defined as being saturated through a majority of the atmosphere with vertical motion exceeding those of a typical synoptic-scale environment, instead resembling speeds consistent with a convective updraft (Durran and Snellman 1987) (Fig. 3). Out of the 216 soundings obtained for all TC supercell cases, this examination revealed 63 soundings with contamination. Many of these cases proved challenging to find a suitable proximity sounding location that was not affected by contamination, especially from saturation. Median values of environmental variables calculated for cases with and without contamination showed considerable differences in variables important for supercells including CAPE, LCL height, and SRH (not shown); therefore, only uncontaminated environments are used hereafter. Environments were also required to be spatiotemporally independent, defined as no more than one representative sounding for cases within 120 km and 3 h of each other (Thompson et al. 2003). This requirement removed 89 soundings, leaving 50 nontornadic and 14 tornadic TC soundings.

Several thermodynamic and kinematic environmental variables are included in our analysis. Thermodynamic variables include mixed-layer (ML) CAPE, most unstable (MU) CAPE, height of the freezing level, and height and temperature of the

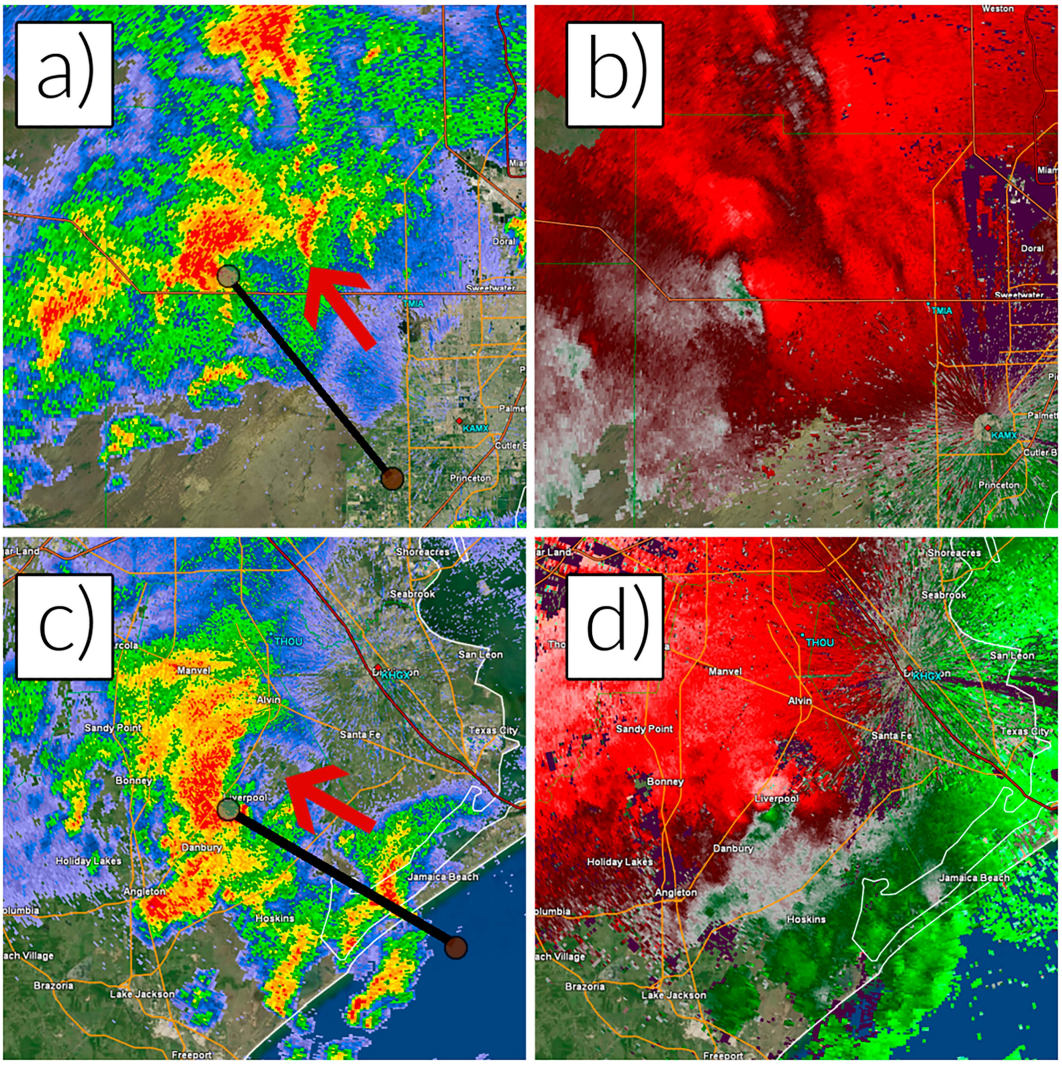

FIG. 2. (a),(b) Example of a NT TC supercell case at 1002 UTC 6 Jun 2013 and (c),(d) a TOR TC supercell case at 0522 UTC 26 Aug 2017. Radar data displayed with GR2Analyst. (a),(c) Base velocity at 0.5° elevation scan with an example of how a RAP model sounding was obtained. The gray dot is located at the tight reflectivity gradient with the red arrow representing the effective inflow layer mean wind direction. The black line follows the 40-km path in the backward direction of the effective inflow layer mean wind, and the brown dot is the sounding location. (b),(d) Base velocity at 0.5° elevation scan.

level of free convection (LFC) (Thompson et al. 2003). Kinematic environmental variables considered include 0–1-, 0–3-, and 0–6-km shear. SRH values were also considered for the 0–1-km layer and 0–3-km layer calculated using Bunkers sounding-derived storm motion (Bunkers et al. 2014). Bunkers motion is a reliable estimate in supercells associated with landfalling TCs (Bunkers et al. 2000; Nowotarski et al. 2021). Observed storm motion was determined for a randomly selected 10% of cases in this study by tracking the distance and direction of the supercell's reflectivity centroid through time using the storm motion tool in the Gibson Ridge Level II (GRLevel2) Analyst software (http://www.grlevelx.com/grlevel2/). The observed storm motion corresponded well with the Bunkers motion (mean absolute error of 5.2° and 2.4 m s^{-1} for storm direction and speed). The supercell composite parameter (SCP) was used to highlight environments with supercell-favorable stability and wind profile conditions. The significant tornado parameter (STP) was also used to highlight favorable environments for supercells with strong tornadoes (Thompson et al. 2003).

c. *Quantifying dual-polarization radar signatures*

Dual-polarization signatures in each supercell were identified and quantified with the Supercell Polarimetric Observation Research Kit (SPORK; Wilson and Van Den Broeke 2021, 2022). This automated algorithm ingests full volumetric WSR-88D data from a single radar site to track and quantify dual-polarization signatures for each individual radar scan.

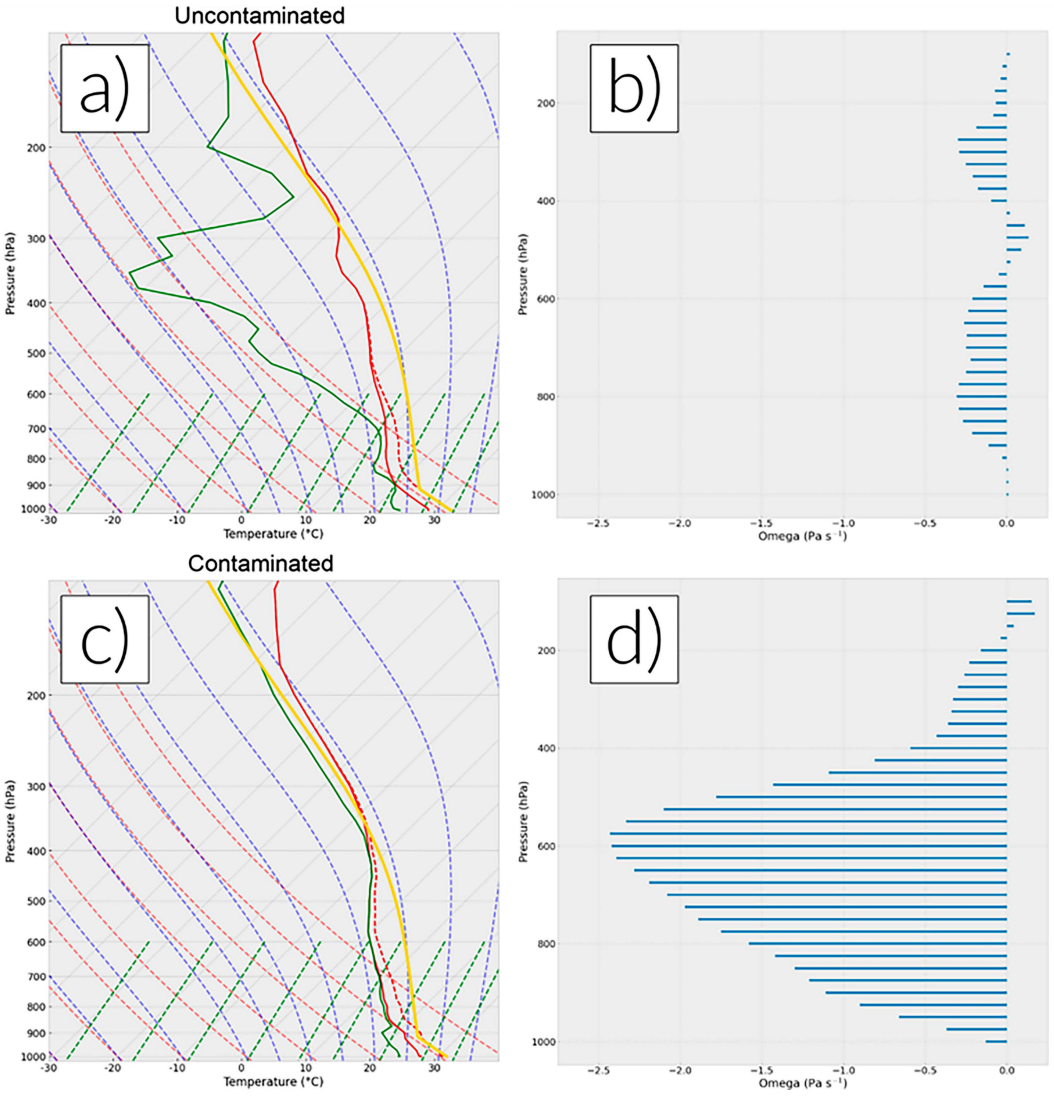

FIG. 3. RAP model (a),(c) skew T soundings and (b),(d) omega values to demonstrate (top) a sounding uncontaminated by nearby overlapping updraft regions (0200 UTC 27 Aug 2011) and (bottom) a sounding that is contaminated (1800 UTC 5 Sep 2019). The solid red line on the skew T is temperature, the solid green line is dewpoint, and the gold line is the parcel lapse rate. Dashed red lines are dry adiabats, and blue dashed lines are moist adiabats. The omega diagram displays omega values by pressure, where negative values indicate rising motion.

The radar data are interpolated onto a 500-m horizontal by 250-m vertical grid. Additional details on preprocessing of data can be found in Wilson and Van Den Broeke (2022). A manually identified forward-flank downdraft (FFD) orientation direction was input for each case (Wilson and Van Den Broeke 2021), allowing the algorithm to identify the inflow side of the supercell for Z_{DR} arc calculations. Due to the known calibration issues with Z_{DR} in the WSR-88D network (Richardson et al. 2017), a Z_{DR} calibration factor was also an input to modify the Z_{DR} field. The Z_{DR} calibration was accomplished using the methodology of Picca and Ryzhkov (2012). Due to the often small and varying nature of dual-polarization signatures in TC supercells, we used the Thunderstorm Risk Estimation from Nowcasting Development via Size Sorting (TRENDSS; Kingfield and Picca 2018) version of the SPORK algorithm. Rather than using a static threshold to identify and contour size-sorting signatures (e.g., Z_{DR} arcs) as SPORK intends to do (Wilson and Van Den Broeke 2021), TRENDSS creates Z_{HH}–Z_{DR} relationships to identify positive Z_{DR} outliers indicative of size sorting. This algorithm is thought to be a more reliable indicator of size-sorting signatures.

For comparisons between tornadic and nontornadic dual-polarization signatures, the analysis period for tornadic supercells is the 30 min prior to the first tornado report. For nontornadic supercells, the analysis period is the 30 min prior to maximum lowest elevation angle NROT (Cooper and Vorst 2016). Median

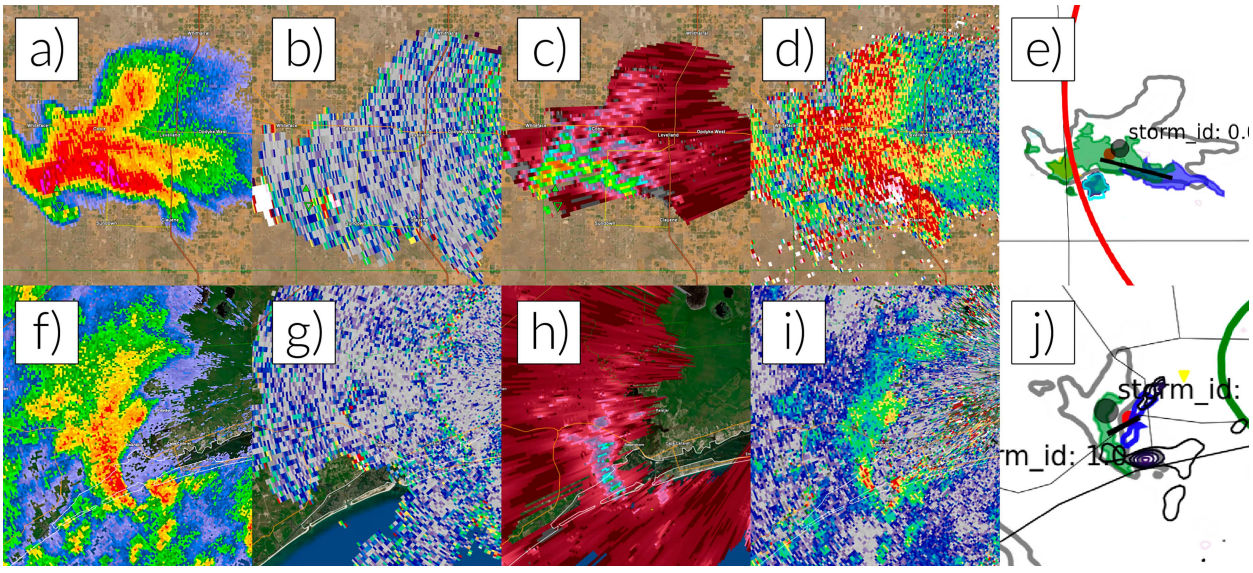

FIG. 4. Radar data and SPORK output for (top) an extratropical TOR supercell at 2228 UTC 19 Jun 2013 and (bottom) TC TOR supercell at 1237 UTC 5 Sep 2019. Radar data displayed with GR2Analyst. (a),(f) Base reflectivity at 0.5° elevation scan. (b),(g) The Z_{DR} field at the 4.0° elevation scan and 15.5° elevation scan to display the Z_{DR} column at approximately 1 km above the environmental freezing level. Note that the TC TOR supercell case does not have a Z_{DR} column. (c),(h) The K_{DP} field at the 0.5° elevation scan. (d),(i) The Z_{DR} field at the 0.5° elevation scan. (e),(j) SPORK output with the gray dots indicating the storm centroids with the storm ID to the northeast, gray contour indicating reflectivity area greater than or equal to 40 dBZ, cyan blue contour surrounding the Z_{DR} column, dark blue contour surrounding the Z_{DR} arc, green contour surrounding the K_{DP} foot, and the thick black line indicating the separation between the Z_{DR} arc and K_{DP} foot.

values of the calculated metrics were examined for the given analysis period. Cases without a consistent MDA detection for the 30 min prior to maximum NROT or first tornado report are excluded from these calculations, leaving 158 nontornadic and 23 tornadic cases. This methodology is consistent with the extratropical comparison dataset (Wilson and Van Den Broeke 2022). Dual-polarization signatures quantified by the SPORK algorithm for each radar scan include the Z_{DR} arc maximum value, Z_{DR} arc mean value, K_{DP}–Z_{DR} separation distance, K_{DP}–Z_{DR} separation angle, Z_{DR} column area, Z_{DR} column maximum depth, and Z_{DR} column mean depth (Fig. 4). The Z_{DR} arc, K_{DP} foot, and K_{DP}–Z_{DR} separation signatures were calculated using 1-km above radar level (ARL) constant-altitude plan position indicators (CAPPIs). The Z_{DR} column signature was calculated at the grid level closest to 1 km above the environmental 0°C level obtained from RAP model soundings. Due to the small size of TC supercells compared to their extratropical counterparts, normalized values were calculated for Z_{DR} column area and K_{DP}–Z_{DR} separation distance to provide additional comparison on a normalized scale. These variables are normalized by the area of the supercell using the reflectivity area > 35 dBZ at the lowest elevation scan. These quantified variables were compared between TC and extratropical supercells and between tornadic and nontornadic TC supercells.

TABLE 3. Dual-polarization signatures recorded with the SPORK algorithm and their corresponding units. The second column indicates whether or not algorithm-reported zero values are removed, and the third column indicates how many supercells exhibited each signature out of the 216 TC cases.

Signature	Zero values removed	Total No. of occurrences in TC cases
Z_{DR} arc maximum value (dB)	Yes	116
Z_{DR} arc mean value (dB)	Yes	116
K_{DP}–Z_{DR} separation distance (km)	Yes	116
K_{DP}–Z_{DR} separation angle (°)	Yes	116
Z_{DR} column area (km^2)	No	41
Z_{DR} column maximum depth (km)	No	41
Z_{DR} column mean depth (km)	No	41

Postprocessing of SPORK output included a few additional measures to ensure high data quality. SPORK outputs a value of zero for very small nonzero values that may be a result of poor WSR-88D resolution or may indicate the absence of a detectable signature. Thus, for all signatures for which zero is unrealistic (e.g., K_{DP}–Z_{DR} separation angle and distance), zero values were not used in statistical comparisons (Table 3). The SPORK algorithm reports Z_{DR} arc and K_{DP} foot mean and maximum values as zero if the signature is not present, so zero values were also not used in statistical comparisons for these signatures. Due to the small and relatively weak nature of TC supercells, it was common for supercells to not exhibit all dual-polarization signatures analyzed by SPORK. Of the 216 TC supercells, 116 had a Z_{DR} arc, 119 had a K_{DP} foot, 41 had a Z_{DR} column, and 9 had hailfall area (Table 3). Both the Z_{DR} arc and K_{DP} foot are required to obtain the K_{DP}–Z_{DR} separation angle and distance—therefore, values were calculated for 116 supercells.

TABLE 4. Environmental variables associated with differences between TC and extratropical supercells (column 1). Median values of TC environments without contamination (column 2) and median values of extratropical supercells (column 3) are shown with the sample size noted in parenthesis, and the WMW p values from the median value comparisons (column 4) with boldface values indicating statistical significance at the 5% level.

Variable	Median, TC (n = 153)	Median, extratropical (n = 206)	WMW p value
LCL (m)	598.3	1035.0	**<0.001**
MLCAPE (J kg^{-1})	1121	1672	**<0.001**
MUCAPE (J kg^{-1})	1978	2256	**0.04**
Freezing-level height (m)	4824.2	3639.1	**<0.001**
0–1-km SRH (m^2 s^{-2})	176.0	147.8	**0.05**
0–3-km SRH (m^2 s^{-2})	244.4	229.2	0.38
0–1-km shear (m s^{-1})	13.6	9.77	**<0.001**
0–3-km shear (m s^{-1})	16.5	16.8	0.18
0–6-km Shear (m s^{-1})	15.9	24.3	**<0.001**
Storm-relative inflow (m s^{-1})	6.7	12.3	**<0.001**

For the TC and extratropical supercell cases, median values of SPORK metrics were calculated for each analysis period (i.e., 30 min prior to tornadogenesis or the maximum base scan NROT) to account for the noise that can be present in these signatures. The median value was selected as it is more outlier resistant than mean. Wilcoxon–Mann–Whitney (WMW) p values were calculated for the comparison of two variables with a null hypothesis that the metric median values could have come from the same distribution. This test was used since distributions could be non-Gaussian, and the WMW test does not require the underlying data to have any particular underlying distribution.

3. Environments of tropical cyclone supercells

This section provides a brief comparison between extratropical and TC supercell environments (Table 4) and a comparison between tornadic and nontornadic TC supercell environments (Table 5). Buoyancy is limited in TC supercell environments since the lapse rate is typically moist adiabatic, leading to lower values of sounding-derived thermodynamic parameters such as MLCAPE and MUCAPE when compared to extratropical supercell environments (Table 4), consistent with prior studies (McCaul 1991; McCaul and Weisman 1996; Davies 2006; Nowotarski et al. 2021). In this study, LCL heights were typically lower in TC supercell environments, while freezing-level heights are significantly higher (Table 4). In terms of kinematic variables, extratropical supercell environments had significantly larger 0–6-km shear (Table 4). TC supercell environments displayed significantly larger 0–1-km shear and SRH values than extratropical environments (McCaul 1991; McCaul and Weisman 1996; Schneider and Sharp 2007; Molinari and Vollaro 2010) (Table 4). However, there is more overlap between tornadic and nontornadic TC supercell cases with these variables than extratropical cases, making it a less reliable indicator of tornadogenesis in TC cases (Table 5).

Differences between tornadic and nontornadic TC environments were minimal (Table 5). Median MLCAPE was significantly larger in tornadic cases (p = 0.03), though overlap existed between the 25th percentile of tornadic cases and 75th percentile of nontornadic cases. Contrasting with prior literature, no significant differences were found between 0–1-km SRH and 0–6-km shear (Davies 2006; Nowotarski et al. 2021). Median SCP and STP are significantly higher in tornadic cases, though there is still overlap in the distributions (not shown).

TABLE 5. Environmental variables for TOR and NT TC supercells without contamination (column 1). Median values of NT cases (column 2) and TOR cases (column 3) with the sample size in parentheses are shown as well as the WMW p values from the median value comparisons (column 4) with boldface values indicating statistical significance at the 5% level.

Variable	Median, NT (n = 132)	Median, TOR (n = 21)	WMW p value
LCL (m)	602.8	586.1	0.89
Level of free convection (m)	731.8	678.2	0.40
MLCAPE (J kg^{-1})	1037	1409	**0.03**
MUCAPE (J kg^{-1})	1904	2428	0.11
SCP	5.9	10.4	**0.03**
STP	1.7	2.6	**0.03**
Freezing-level height (m)	4842.8	4800.1	0.69
0–1-km SRH (m^2 s^{-2})	167.3	191.8	0.40
0–3-km SRH (m^2 s^{-2})	235.4	270.6	0.33
0–1-km shear (m s^{-1})	13.6	13.4	0.99
0–3-km shear (m s^{-1})	16.7	16.2	0.31
0–6-km shear (m s^{-1})	15.4	17.9	0.37
Storm-relative inflow (m s^{-1})	6.5	7.1	0.52

TABLE 6. Extratropical and TC supercell median values of dual-polarization radar metrics (column 1) for NT cases (columns 2–3) and TOR cases (columns 5–6) with the sample size notes in parentheses. Corresponding WMW p values between NT extratropical and TC cases are displayed in column 4, while WMW p values for TOR cases are displayed in column 7 with boldface values indicating statistical significance at the 5% level.

	NT			TOR		
Variable	Midlatitude	TC	WMW p value	Midlatitude	TC	WMW p value
Z_{DR} column area (km^2)	23.153 (n = 79)	2.947 (n = 35)	**<0.001**	33.917 (n = 91)	4.441 (n = 6)	**<0.001**
Normalized Z_{DR} column area	0.048 (n = 79)	0.010 (n = 35)	**<0.001**	0.070 (n = 91)	0.033 (n = 6)	**0.019**
Z_{DR} column mean depth (km)	1.578 (n = 79)	0.560 (n = 35)	**<0.001**	1.717 (n = 91)	1.269 (n = 6)	**0.004**
Z_{DR} column maximum depth (km)	3.000 (n = 79)	1.500 (n = 35)	**<0.001**	3.250 (n = 91)	1.563 (n = 6)	**<0.001**
Z_{DR} arc mean value (dB)	3.656 (n = 78)	4.018 (n = 96)	**<0.001**	3.668 (n = 90)	3.977 (n = 20)	**<0.001**
Z_{DR} arc maximum value (dB)	4.635 (n = 78)	5.329 (n = 96)	**<0.001**	4.578 (n = 90)	5.318 (n = 20)	**<0.001**
K_{DP}–Z_{DR} separation distance (km)	7.303 (n = 78)	5.246 (n = 96)	**<0.001**	7.097 (n = 90)	5.180 (n = 20)	**<0.001**
Normalized K_{DP}–Z_{DR} separation distance	0.016 (n = 78)	0.018 (n = 96)	0.060	0.013 (n = 90)	0.025 (n = 20)	**0.006**
K_{DP}–Z_{DR} separation angle (°)	27.608 (n = 78)	115.892 (n = 96)	**<0.001**	69.777 (n = 90)	101.927 (n = 20)	**<0.001**

4. Comparing radar signatures of tropical cyclone and midlatitude supercells

Establishing differences between dual-polarization signatures in extratropical and TC supercells can improve understanding of how the extratropical model of supercell radar signatures needs to be modified for application to TC supercells. Prior literature established that TC supercells are typically smaller in horizontal and vertical extent when compared to their extratropical counterparts (Edwards 2012), and these differences should be seen in their dual-polarization signatures. Established environmental differences may also promote contrasting dual-polarization signature characteristics between extratropical and TC supercells.

Median values of tornadic (TOR) and nontornadic (NT) dual-polarization signatures in extratropical and TC cases and their corresponding WMW p values are displayed in Table 6. Both Z_{DR} column area and normalized Z_{DR} column area were significantly smaller in TC supercells than extratropical supercells, including both TOR and NT ($p = 0.02$ and $p < 0.001$, respectively) (Table 6; Fig. 5). The Z_{DR} columns were infrequent in TC supercells compared to extratropical cases. Extratropical cases had Z_{DR} columns in 94.0% and 95.8% of NT and TOR cases, respectively. Meanwhile, TC cases had Z_{DR} columns in only 18.2% and 25.0% of NT and TOR cases, respectively. The common absence of Z_{DR} columns in TC cases leaves a small sample size of only six TC TOR cases with a Z_{DR} column for the analysis. These results are investigated further in the next section.

Mean and maximum Z_{DR} column depth were significantly smaller in TC supercells than in extratropical supercells, and only 41 TC cases had this signature. Median Z_{DR} column maximum depth was nearly twice as large in extratropical supercells than in TC supercells (Fig. 6). More variation was seen between extratropical and TC cases with mean Z_{DR} column depth; however, mean Z_{DR} column depth in both nontornadic and tornadic extratropical supercells was found to be significantly larger than in TC supercells ($p < 0.001$ and $p = 0.01$, respectively; Table 6). The shallower Z_{DR} columns in TC supercells likely stems from the higher freezing levels in TC environments (~1200 m; Table 4), requiring the air to be lofted to higher levels in TC supercells to get a Z_{DR} column. Additionally, CAPE values were substantially larger in extratropical supercell environments (by 300–500 J kg^{-1}; Table 4), suggesting that updrafts in TC supercells are less driven by instability. These environmental factors lead to the expectation that Z_{DR} columns will be shallower and weaker in TC supercells. The drop size distributions (DSDs) in tropical environments shift toward smaller drops compared to midlatitude cases (Deo and Walsh 2016; Chen et al. 2017; Hopper et al. 2019), which can reduce Z_{DR} of lofted drops above the higher freezing levels, ultimately leading to shallower and less prominent Z_{DR} columns.

The Z_{DR} arcs are also less frequent in TC supercells than in extratropical supercells. In extratropical supercells, Z_{DR} arcs appeared in 92.9% and 94.7% of NT and TOR supercells, respectively. However, only 50.0% and 83.3% of NT and TOR TC supercells, respectively, featured this signature. The Z_{DR} arc mean and maximum values were significantly larger in TC cases than in extratropical cases (e.g., $p < 0.001$ for arc mean; Table 6; Fig. 7). This result contrasts with what is known about tropical DSDs when compared to extratropical DSDs. Tropical DSDs typically contain a large concentration of small drops corresponding to lower Z_{DR} values (Tokay et al. 2008; Thompson et al. 2018). Since the concentration of particles does not affect Z_{DR}, it may only take a small number of large drops being advected by the stronger low-level wind

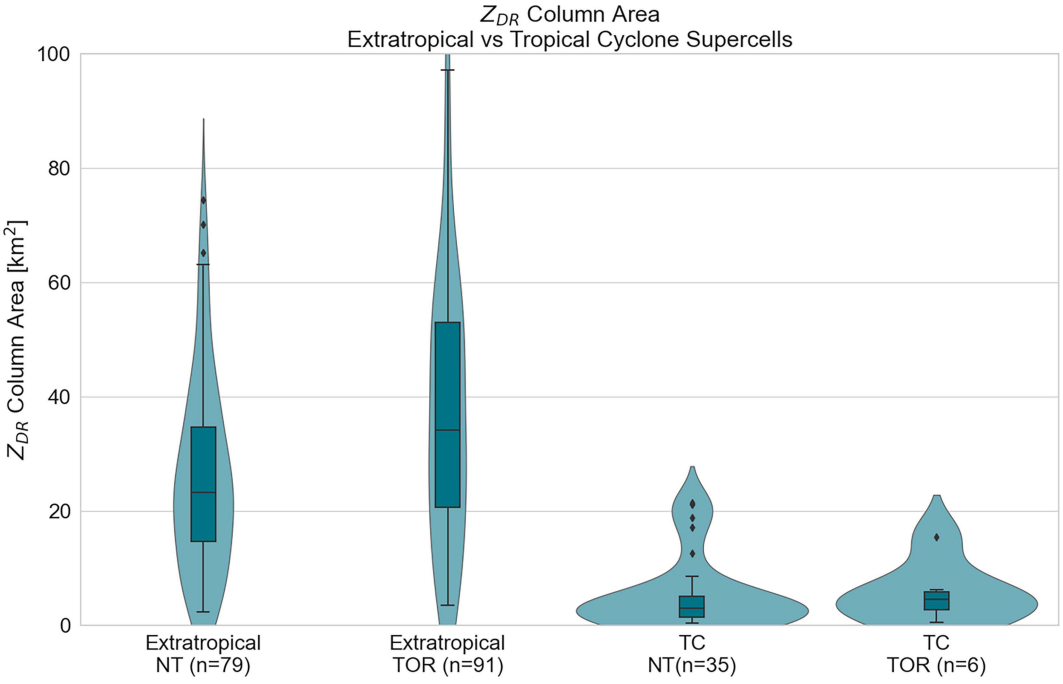

FIG. 5. Violin plot displaying the distribution of Z_{DR} column area (km^2) for (left) extratropical NT supercells, (middle left) extratropical TOR supercells, (middle right) TC NT supercells, and (right) TC TOR supercells. Valid for 30 min prior to the maximum NROT for NT cases or the first tornado report for TOR cases. The number of samples contributing to each violin is indicated on the axis labels. Box-and-whisker plots are embedded in violin plots with boxes displaying the 25th and 75th percentile with the black horizontal line indicating the median value. Whiskers indicate the 10th and 90th percentile with the outliers represented by black diamonds.

shear and higher 0–1-km SRH in TC cases to create and enhance the Z_{DR} arc.

Differences are prominent between both K_{DP} foot and Z_{DR} arc separation angle and distance in extratropical and TC supercells. Normalized separation distance is significantly larger in TOR and slightly larger in NT TC cases than in extratropical cases ($p < 0.01$ and $p = 0.06$, respectively; Table 6; Fig. 8). Separation angle remains significantly larger in TC

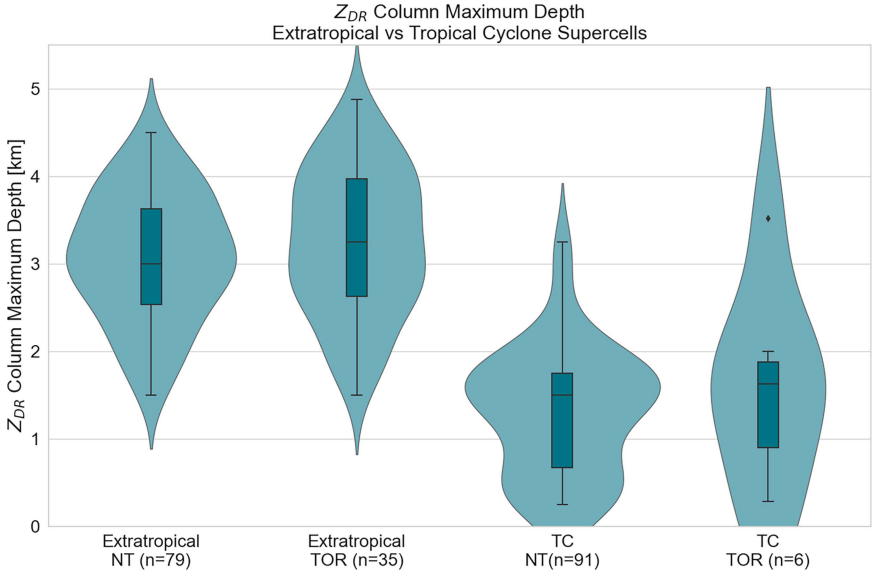

FIG. 6. As in Fig. 5, but for Z_{DR} column maximum depth.

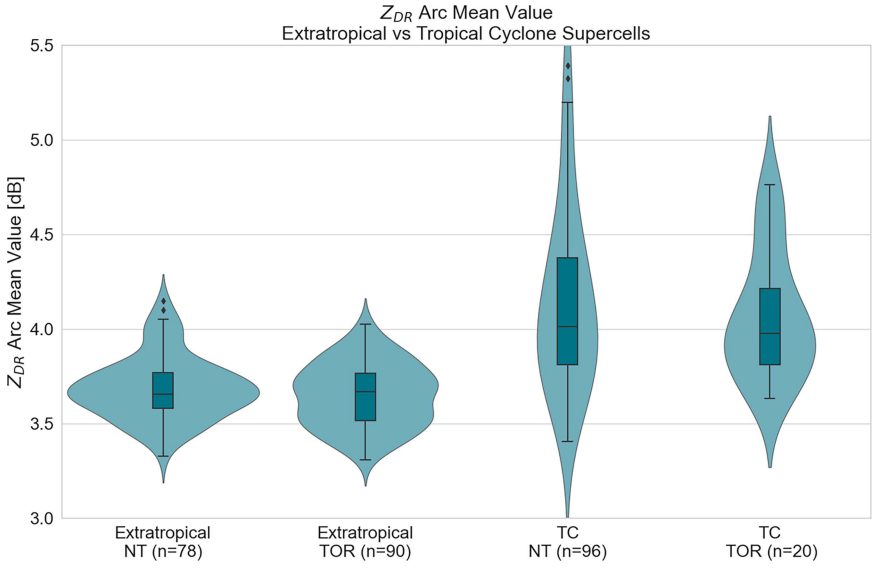

FIG. 7. As in Fig. 5, but for Z_{DR} arc mean value.

supercells when compared to that in extratropical supercells. The increased low-level wind shear and 0–1-km SRH in TC environments may be responsible for this larger normalized separation distance and angle between the K_{DP} foot and Z_{DR} arc.

5. Comparing radar signatures of tropical cyclone tornadic and nontornadic supercells

Median values of dual-polarization signatures in TOR and NT TC supercells are compared in this section (Table 7). This analysis utilized the 30 min prior to the first tornado report for TOR cases and 30 min prior to the maximum NROT for NT cases. Neither Z_{DR} column area nor normalized Z_{DR} column area displayed significant differences between NT and TOR supercells ($p = 0.59$ and $p = 0.27$, respectively). The Z_{DR} column mean depth was only slightly larger in TOR cases compared to that in NT cases ($p = 0.07$), and maximum Z_{DR} column depth was similar between NT and TOR cases ($p = 0.68$). These results contrast with prior findings from extratropical supercells which found larger Z_{DR} column area and depth in TOR supercells when compared to that in NT extratropical supercells (Van Den Broeke 2017, 2020; French and Kingfield 2021). This difference may be due to tornadic TC cases typically producing weak, short-lived EF0 or EF1 tornadoes. These distinctions may be more apparent in intense tornadoes, rather than in comparisons between weakly

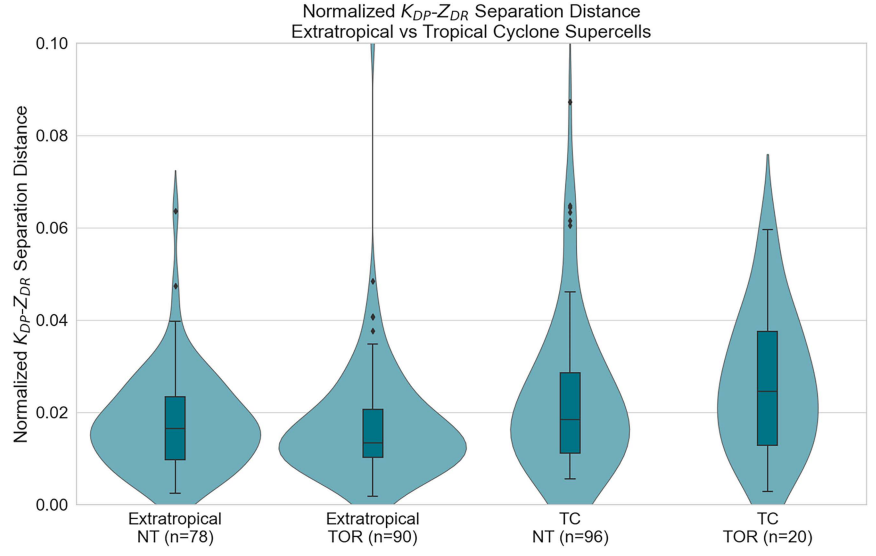

FIG. 8. As in Fig. 5, but for normalized K_{DP}–Z_{DR} separation distance.

TABLE 7. TC supercell dual-polarization radar metric (column 1) median values for NT supercells (column 2) and TOR supercells (column 3) from Table 6 and WMW p values for a comparison of the NT and TOR distributions (column 4).

Variable	NT	TOR	WMW p value
Z_{DR} column area (km^2)	2.95	4.44	0.59
Normalized Z_{DR} column area	0.01	0.03	0.27
Z_{DR} column mean depth (km)	0.56	1.27	0.07
Z_{DR} column maximum depth (km)	1.50	1.56	0.68
Z_{DR} arc mean value (dB)	4.02	3.98	0.70
Z_{DR} arc maximum value (dB)	5.33	5.32	0.65
K_{DP}–Z_{DR} separation distance (km)	5.25	5.18	0.41
K_{DP}–Z_{DR} separation angle (°)	115.89	101.93	0.18

tornadic and nontornadic cases (Markowski et al. 2002). It is also possible that the extratropical supercells analyzed in prior studies were more discrete.

The lack of Z_{DR} column signatures in TC cases (18.2% of NT cases, 25.0% of TOR cases) warrants further investigation. As discussed previously, past work can be used to infer that high freezing levels, lower values of CAPE, and low LCL heights in TC environments may explain why these signatures occur infrequently in TC supercells. TC environments exhibited median freezing levels significantly higher (by nearly 1200 m) than their extratropical counterparts ($p < 0.001$; Table 4). However, no significant difference was found between the freezing levels of TC cases with Z_{DR} columns and those without ($p = 0.88$). Additionally, median LCL heights in TC environments were, on average, nearly 500 m lower than in extratropical environments ($p < 0.001$; Table 4), supporting the idea of Mulholland et al. (2021) that lower LCL heights contribute to smaller updraft areas. The significantly weaker 0–6-km shear in TC environments ($p < 0.001$; Table 4) further supports the hypothesis of smaller updrafts and, therefore, smaller Z_{DR} columns in TC supercells (Warren et al. 2017; Peters et al. 2019, 2020).

The Z_{DR} arc maximum and mean values were similar between tornadic and nontornadic cases ($p = 0.65$ and $p = 0.70$, respectively). However, prior work using a smaller sample size found a larger Z_{DR} arc magnitude in tornadic TC supercells (Crowe et al. 2009). Median values of separation distance between the K_{DP} foot and Z_{DR} arc were approximately 5 km in both NT and TOR cases (Table 7), with no significant difference between NT and TOR cases ($p = 0.41$). Separation angle between the K_{DP} foot and Z_{DR} arc was large in TC cases, with median values $> 100°$ in both NT and TOR cases. There were no significant differences in the K_{DP}–Z_{DR} separation angle between NT and TOR cases ($p = 0.18$). These results reject our hypothesis that the K_{DP}–Z_{DR} separation angle and distance will be larger in TOR cases.

Spearman's rank-order correlations between environmental parameters and dual-polarization variables metrics were also calculated to determine if dual-polarization variables vary by environment (Table 8). Spearman's rank-order correlation was chosen as it allows for a monotonic relationship, i.e., a relationship between two variables in which one increases or decreases in response to changes in the other. Spearman's rank-order correlation indicates that Z_{DR} column area and mean depth are associated with higher LCL and LFC height ($r = 0.30$ and $r = 0.32$ for Z_{DR} column area, $r = 0.38$ and $r = 0.30$ for Z_{DR} column mean depth, respectively; Table 8). Low Spearman's rank-order correlation was found between Z_{DR} column area/depth and MUCAPE/MLCAPE. This contrasts with prior results for extratropical supercells [e.g., Wilson and Van Den Broeke (2022) found that Z_{DR} column area and depth have a moderate positive Spearman's rank-order correlation with MUCAPE and MLCAPE].

Maximum NROT in the three lowest elevation angles per volume scan can be used as a proxy for low-level mesocyclone strength (Turnage 2014; Cooper and Vorst 2016). An initial quality check was done to determine if NROT was correlated with distance from the radar and radar elevation angle. This quality check helps to ensure that NROT is a justifiable proxy

TABLE 8. Spearman's rank-order correlations between uncontaminated RAP sounding environmental parameters and both NT and TOR TC dual-polarization variables. Correlations with magnitude ≥ 0.30 are bolded.

Environmental variable	Z_{DR} column area	Z_{DR} column mean depth	Z_{DR} column maximum depth	K_{DP}–Z_{DR} separation distance	K_{DP}–Z_{DR} separation angle
LCL height (m)	**0.30**	**0.38**	0.13	0.02	−0.00
LFC height (m)	**0.32**	**0.30**	0.17	0.07	0.07
MLCAPE (J kg^{-1})	−0.12	0.18	−0.12	−0.03	0.06
MUCAPE (J kg^{-1})	−0.19	0.14	−0.18	−0.01	0.08
CIN (J kg^{-1})	**−0.32**	**−0.31**	−0.28	−0.06	−0.05
SCP	0.11	0.04	0.20	−0.04	0.03
STP	0.11	0.06	0.24	−0.03	0.00
Freezing-level height (m)	−0.03	−0.05	−0.08	0.08	0.07
Effective SRH (m^2 s^{-2})	0.19	0.03	0.18	−0.04	0.04
0–1-km SRH (m^2 s^{-2})	0.27	0.03	0.24	0.03	0.03
0–3-km SRH (m^2 s^{-2})	**0.33**	0.08	**0.32**	0.01	0.06
0–1-km shear (kt; 1 kt ≈ 0.51 m s^{-1})	0.14	−0.04	0.27	−0.13	0.18
0–3-km shear (kt)	**0.34**	0.8	**0.41**	−0.07	0.13
0–6-km shear (kt)	0.04	−0.16	0.01	−0.03	−0.24

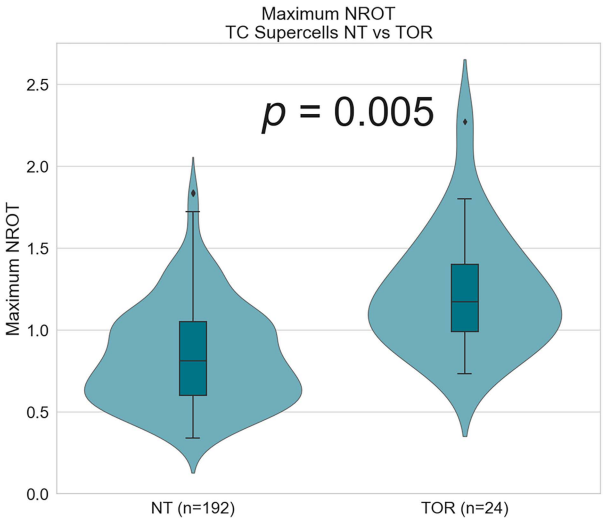

FIG. 9. Violin plots displaying the maximum NROT for (left) NT and (right) TOR TC supercells. The number of samples contributing to each violin is indicated on the horizontal axis label. Box-and-whisker plots are embedded in violin plots with boxes displaying the 25th and 75th percentile and the black horizontal line indicating the median value. Whiskers convey the 10th and 90th percentile with the outliers represented by black diamonds.

for low-level mesocyclone strength. For both TOR and NT cases, low Pearson's correlation was found between NROT and distance from the radar ($r = 0.05$ and $r = 0.02$, respectively). Low correlation was also found between NROT and radar elevation angle for both TOR and NT cases ($r = 0.28$ and $r = 0.35$, respectively), explaining approximately 10% of the variation in NROT. Through this analysis, it was determined that NROT values were not strongly correlated with distance from the radar and radar elevation angle and, therefore, are a justifiable proxy for low-level mesocyclone strength.

Maximum NROT was obtained for all 192 NT and 24 TOR TC supercells. These values were obtained from the time of peak NROT for NT cases or the time closest to the first tornado report for TOR cases. Tornadic TC supercells had significantly larger maximum NROT values ($p = 0.01$; Fig. 9). Median NROT value for NT TC supercells was 0.810, while this value increased to 0.992 for TOR cases, a statistically significant difference ($p = 0.005$). This result is expected since prior literature indicates that tornadic mesocyclones are stronger than nontornadic mesocyclones in TC supercells (Schneider and Sharp 2007; Martinaitis 2017).

6. Summary and discussion

Establishing differences in dual-polarization signatures between well-studied extratropical and underresearched TC supercells is important for the interpretation and application of these signatures in TC supercells. There were large differences between dual-polarization signatures in extratropical and TC supercells.

The Z_{DR} columns were less common in TC supercell cases and, when present, exhibited a reduced size and depth. The absence of Z_{DR} columns is likely due to a combination of the high environmental freezing level, lower LCL heights, and shallower depth of TC supercells, making raindrops or water-coated ice particles uncommon above the freezing level (Kumjian et al. 2014; Snyder et al. 2015; Mulholland et al. 2021). The increased ground-relative velocity of TC supercells could also cause these supercells to have an unrepresentative tilted appearance between radar scans at different elevation angles, minimizing the ability to detect Z_{DR} columns. This is a known limitation of the SPORK algorithm (Wilson and Van Den Broeke 2022). In TC cases for which Z_{DR} columns are present, the signature is shallow, small in areal extent, and shows little variation in area or depth with time. The reduced size and depth of Z_{DR} columns in TC supercells when compared to their extratropical counterparts may be partially driven by their lower LCL heights, which promote shallower and narrower updrafts (Mulholland et al. 2021). Weaker updrafts and, therefore, smaller Z_{DR} columns, in TC cases, may also be due to the weaker deep-layer shear and consequently the weaker low-level storm-relative winds in TC environments (Warren et al. 2017; Peters et al. 2019, 2020). The substantially weaker CAPE in TC environments also indicates that the updrafts are not going to be driven as strongly by instability. These factors combined support the expectation that Z_{DR} columns will be shallower in TC supercells when compared to extratropical supercells. Due to TC supercells exhibiting little variation in Z_{DR} column area or depth in time, this signature does not appear to give an indication of a TC supercell's tornadic potential as it may in extratropical cases (Van Den Broeke 2017, 2020; French and Kingfield 2021).

A key result is the difference in low-level mesocyclone strength between tornadic and nontornadic TC supercells. Tornadic TC supercells had significantly larger NROT values at the time of initial tornadogenesis than nontornadic TC supercells at the time of maximum low-level rotation, indicating that tornadic TC supercells typically have stronger low-level mesocyclones. The stronger NROT values in tornadic TC cases compared to nontornadic cases agrees with Schneider and Sharp (2007) and Martinaitis (2017) who detected stronger mesocyclones in tornadic TC supercells. With additional work investing low-level mesocyclone strength prior and during tornadogenesis with a larger sample size of TC tornadic cases, the result that tornadic TC supercells have stronger low-level mesocyclones than their nontornadic counterparts may be important for operational meteorologists when gauging tornadic potential in TC supercells.

Although less common than their extratropical counterparts, Z_{DR} arcs were observed slightly more than half of TC supercells. Mean and maximum Z_{DR} values within this signature were typically larger than those of their extratropical counterparts. We hypothesize that the stronger low-level wind shear and higher 0–1-km SRH in TC cases promote more effective drop-size sorting and, therefore, helps to create and enhance the Z_{DR} arc (Kumjian and Ryzhkov 2009; Van Den Broeke 2016). The increased magnitude of the Z_{DR} arc in TC cases was not expected given that TC DSDs typically consist of a high concentration of small drops (Deo and Walsh 2016; Chen et al. 2017; Hopper et al. 2019). It could be speculated that the deep warm-cloud layer in TC supercells facilitated enhanced droplet

growth through collision and coalescence, leading to the enhanced values in the Z_{DR} arc (Berry and Reinhardt 1974; Feingold et al. 1996). Neither the mean nor maximum values within the signature indicate the tornadic potential of a TC supercell. This finding contrasts with Crowe et al. (2009) who observed larger Z_{DR} arc values in tornadic TC supercells than nontornadic supercells in Hurricane Rita (2005).

Separation angle between the K_{DP} foot and Z_{DR} arc is significantly larger in TC cases than extratropical cases. This is also likely due to the increased low-level wind shear and 0–1-km SRH in TC cases promoting more effective size sorting (Crowe et al. 2009; Loeffler and Kumjian 2020). While the separation angle between the K_{DP} foot and Z_{DR} arc appeared larger in TC cases, separation distance was still larger in extratropical cases. Separation distance or angle did not give insight into the tornadic potential of TC supercells. This result contrasts with that of Crowe et al. (2009) and Martinaitis (2017) who observed a larger separation distance between the K_{DP} foot and Z_{DR} arc in tornadic TC supercells. However, Loeffler et al. (2020) found similar separation distance between the K_{DP} foot and Z_{DR} arc in extratropical tornadic versus nontornadic cases. The lack of any significant differences between the K_{DP} foot and Z_{DR} separation distance and angle between tornadic and nontornadic TC supercells could be explained by the lack of environmental differences between the two. Prior work has associated an increase in SRH and storm-relative flow with increased separation distance and more orthogonal separation angles (Loeffler and Kumjian 2020; Loeffler et al. 2023). Environmental analysis provided no significant differences in these kinematic variables between tornadic and nontornadic TC supercells, perhaps limiting any difference in size-sorting processes and, therefore, separation between the signatures.

This study found stronger mesocyclones in tornadic cases but no differences in any signature related to size-sorting processes. The lack of differences may be a result of tornadic TC cases remaining weakly tornadic, typically producing short-lived EF0 or EF1 tornadoes. Perhaps, these differences would be more evident if intense tornadoes rather than weakly tornadic cases were compared with nontornadic cases (Markowski et al. 2002). Additionally, since these supercells are shallow, the radar beam height may also be above the level at which size-sorting processes are taking place, even within the 100-km range required for this study. Operational meteorologists should be aware of the apparent limited use of dual-polarization signatures when making warning decisions on TC supercells.

Future work should focus on differences in dual-polarization signatures between tornadic and nontornadic TC supercells with a larger sample size of tornadic cases (when possible) to improve statistical robustness. Differences observed in this study may motivate additional investigations utilizing rapid-scan and/or high-resolution radar data to analyze how dual-polarization signatures evolve over time in both tornadic and nontornadic TC supercells. Additionally, numerical study of supercells in TC environments paired with dual-polarization emulation may also provide valuable insight, as many observations of mesocyclone strength are throughout interactions with the coastline and baroclinic boundaries. Attention should also be focused on radar signatures as a function of supercell distance from the TC center, since supercells farther from the TC center are more dependent on the ambient environment (Schultz and Cecil 2009). Additional work should also seek to better quantify and predict small-scale inhomogeneity in variables such as SRH and 0–1-km shear in TC environments.

Acknowledgments. The authors thank Matt Wilson for his help with the SPORK algorithm and George Limpert for the development of the MDA. The lead author was supported by NOAA Grant NA19OAR4590340 and USDA Grant USDA-NIFA-TCRGP-006773.

Data availability statement. The dataset used in this paper was obtained online (radar data: https://s3.amazonaws.com/noaa-nexrad-level2/index.html; RAP data: https://www.nco.ncep.noaa.gov/pmb/products/rap/; Storm Events Database: https://www.ncdc.noaa.gov/stormevents/).

REFERENCES

Benjamin, S. G., and Coauthors, 2016: A North American hourly assimilation and model forecast cycle: The Rapid Refresh. *Mon. Wea. Rev.*, **144**, 1669–1694, https://doi.org/10.1175/MWR-D-15-0242.1.

Berry, E. X., and R. L. Reinhardt, 1974: An analysis of cloud drop growth by collection: Part I. Double distributions. *J. Atmos. Sci.*, **31**, 1814–1824, https://doi.org/10.1175/1520-0469(1974)031<1814:AAOCDG>2.0.CO;2.

Blumberg, W. G., K. T. Halbert, T. A. Supinie, P. T. Marsh, R. L. Thompson, and J. A. Hart, 2017: SHARPpy: An open-source sounding analysis toolkit for the atmospheric sciences. *Bull. Amer. Meteor. Soc.*, **98**, 1625–1636, https://doi.org/10.1175/BAMS-D-15-00309.1.

Bunkers, M. J., B. A. Klimowski, J. W. Zeitler, R. L. Thompson, and M. L. Weisman, 2000: Predicting supercell motion using a new hodograph technique. *Wea. Forecasting*, **15**, 61–79, https://doi.org/10.1175/1520-0434(2000)015<0061:PSMUAN>2.0.CO;2.

——, ——, D. A. Barber, R. L. Thompson, R. Edwards, and J. Garner, 2014: Choosing a universal mean wind for supercell motion prediction. *J. Oper. Meteor.*, **2**, 115–129, https://doi.org/10.15191/nwajom.2014.0211.

Carlin, J. T., and A. V. Ryzhkov, 2019: Estimation of melting-layer cooling rate from dual-polarization radar: Spectral bin model simulations. *J. Appl. Meteor. Climatol.*, **58**, 1485–1508, https://doi.org/10.1175/JAMC-D-18-0343.1.

Chen, B., Z. Hu, L. Liu, and G. Zhang, 2017: Raindrop size distribution measurements at 4,500 m on the Tibetan Plateau during TIPEX-III. *J. Geophys. Res. Atmos.*, **122**, 11 092–11 106, https://doi.org/10.1002/2017JD027233.

Conway, J. W., K. D. Hondl, M. J. Moreland, J. M. Cordell, and R. J. Harron, 1995: Improvements in the WSR-88D dealiasing algorithm: The pursuit of the final, most important gates. Preprints, *27th Conf. on Radar Meteorology*, Vail, CO, Amer. Meteor. Soc., 145–147.

Cooper, D. T., and A. B. Vorst, 2016: Assessing the utility of normalized rotation in detecting tornado development in the Allegheny front. *Proc. Northeast Regional Operational Workshop XVII*, Albany, NY, NOAA and NWS, 21 pp., https://www.weather.gov/media/rlx/NROTpresentation.pdf.

Crowe, C. C., W. A. Petersen, and L. D. Carey, 2009: A dual-polarization investigation of tornado warned cells associated with Hurricane Rita (2005). *34th Conf. on Radar Meteorology*, Williamsburg, VA, Amer. Meteor. Soc., P13.7, https://ams.confex.com/ams/pdfpapers/155314.pdf.

——, C. J. Schultz, M. Kumjian, L. D. Carey, and W. A. Petersen, 2012: Use of dual-polarization signatures in diagnosing tornadic potential. *Electron. J. Oper. Meteor.*, **13**, 57–87.

Davies, J., 1990: Midget supercell spawns tornadoes. *Weatherwise*, **43**, 260, https://doi.org/10.1080/00431672.1990.9929350.

——, 2006: Hurricane and tropical cyclone tornado environments from RUC proximity soundings. Preprints, *23rd Conf. on Severe Local Storms*, St. Louis, MO, Amer. Meteor. Soc., 12.6A, https://ams.confex.com/ams/pdfpapers/115483.pdf.

Dawson, D. T., II, E. R. Mansell, Y. Jung, L. J. Wicker, M. R. Kumjian, and M. Xue, 2014: Low-level Z_{DR} signatures in supercell forward flanks: The role of size sorting and melting of hail. *J. Atmos. Sci.*, **71**, 276–299, https://doi.org/10.1175/JAS-D-13-0118.1.

——, ——, and M. R. Kumjian, 2015: Does wind shear cause hydrometeor size sorting? *J. Atmos. Sci.*, **72**, 340–348, https://doi.org/10.1175/JAS-D-14-0084.1.

Deo, A., and K. J. E. Walsh, 2016: Contrasting tropical cyclone and non-tropical cyclone related rainfall drop size distribution at Darwin, Australia. *Atmos. Res.*, **181**, 81–94, https://doi.org/10.1016/j.atmosres.2016.06.015.

Devanas, A. D., D. Gregoria, K. B. Kasper, and P. Santos, 2008: Tropical cyclone induced tornadoes associated with the formation of Tropical Storm Barry. *Tropical Meteorology Special Symp./20th Conf. on Climate Variability and Change*, New Orleans, LA, Amer. Meteor. Soc., JP3.16, https://ams.confex.com/ams/pdfpapers/131758.pdf.

Durran, D. R., and L. W. Snellman, 1987: The diagnosis of synoptic-scale vertical motion in an operational environment. *Wea. Forecasting*, **2**, 17–31, https://doi.org/10.1175/1520-0434(1987)002<0017:TDOSSV>2.0.CO;2.

Edwards, R., 2012: Tropical cyclone tornadoes: A review of knowledge in research and prediction. *Electron. J. Severe Storms Meteor.*, **7** (6), https://doi.org/10.55599/ejssm.v7i6.42.

Eilts, M. D., and S. D. Smith, 1990: Efficient dealiasing of Doppler velocities using local environment constraints. *J. Atmos. Oceanic Technol.*, **7**, 118–128, https://doi.org/10.1175/1520-0426(1990)007<0118:EDODVU>2.0.CO;2.

Feingold, G., W. R. Cotton, B. Stevens, and A. S. Frisch, 1996: The relationship between drop in-cloud residence time and drizzle production in numerically simulated stratocumulus clouds. *J. Atmos. Sci.*, **53**, 1108–1122, https://doi.org/10.1175/1520-0469(1996)053<1108:TRBDIC>2.0.CO;2.

French, M. M., and D. M. Kingfield, 2021: Tornado formation and intensity prediction using polarimetric radar estimates of updraft area. *Wea. Forecasting*, **36**, 2211–2231, https://doi.org/10.1175/WAF-D-21-0087.1.

Healey, D. J., and M. S. Van Den Broeke, 2023: Comparing polarimetric signatures of proximate pretornadic and nontornadic supercells in similar environments. *Wea. Forecasting*, **38**, 2011–2027, https://doi.org/10.1175/WAF-D-23-0013.1.

Herzegh, P. H., and A. R. Jameson, 1992: Observing precipitation through dual-polarization radar measurements. *Bull. Amer. Meteor. Soc.*, **73**, 1365–1376, https://doi.org/10.1175/1520-0477(1992)073<1365:OPTDPR>2.0.CO;2.

Hopper, L. J., Jr., C. Schumacher, K. Humes, and A. Funk, 2019: Drop-size distribution variations associated with different storm types in southeast Texas. *Atmosphere*, **11**, 8, https://doi.org/10.3390/atmos11010008.

Kingfield, D. M., and J. C. Picca, 2018: Development of an operational convective nowcasting algorithm using raindrop size sorting information from polarimetric radar data. *Wea. Forecasting*, **33**, 1477–1495, https://doi.org/10.1175/WAF-D-18-0025.1.

Knupp, K. R., J. R. Stalker, and E. W. McCaul Jr., 1998: An observational and numerical study of a mini-supercell storm. *Atmos. Res.*, **49**, 35–63, https://doi.org/10.1016/S0032-5910(97)93378-7.

Kumjian, M. R., 2013: Principles and applications of dual-polarization weather radar. Part I: Description of the polarimetric radar variables. *J. Oper. Meteor.*, **1**, 226–242, https://doi.org/10.15191/nwajom.2013.0119.

——, and A. V. Ryzhkov, 2007: Polarimetric characteristics of tornadic and nontornadic supercell thunderstorms. Preprints, *33rd Conf. on Radar Meteorology*, Cairns, QLD, Australia, Amer. Meteor. Soc., P10.1, https://ams.confex.com/ams/33Radar/webprogram/Paper122882.html.

——, and ——, 2008: Polarimetric signatures in supercell thunderstorms. *J. Appl. Meteor. Climatol.*, **47**, 1940–1961, https://doi.org/10.1175/2007JAMC1874.1.

——, and ——, 2009: Storm-relative helicity revealed from polarimetric radar measurements. *J. Atmos. Sci.*, **66**, 667–685, https://doi.org/10.1175/2008JAS2815.1.

——, and ——, 2012: The impact of size sorting on the polarimetric radar variables. *J. Atmos. Sci.*, **69**, 2042–2060, https://doi.org/10.1175/JAS-D-11-0125.1.

——, ——, V. M. Melnikov, and T. J. Schuur, 2010: Rapid-scan super-resolution observations of a cyclic supercell with a dual-polarization WSR-88D. *Mon. Wea. Rev.*, **138**, 3762–3786, https://doi.org/10.1175/2010MWR3322.1.

——, A. P. Khain, N. Benmoshe, E. Ilotoviz, A. V. Ryzhkov, and V. T. J. Phillips, 2014: The anatomy and physics of Z_{DR} columns: Investigating a polarimetric radar signature with a spectral bin microphysical model. *J. Appl. Meteor. Climatol.*, **53**, 1820–1843, https://doi.org/10.1175/JAMC-D-13-0354.1.

Loeffler, S. D., and M. R. Kumjian, 2020: Idealized model simulations to determine impacts of storm-relative winds on differential reflectivity and specific differential phase fields. *J. Geophys. Res. Atmos.*, **125**, e2020JD033870, https://doi.org/10.1029/2020JD033870.

——, ——, M. Jurewicz, and M. M. French, 2020: Differentiating between tornadic and nontornadic supercells using polarimetric radar signatures of hydrometeor size sorting. *Geophys. Res. Lett.*, **47**, e2020GL088242, https://doi.org/10.1029/2020GL088242.

——, ——, P. M. Markowski, B. E. Coffer, and M. D. Parker, 2023: Investigating the relationship between polarimetric radar signatures of hydrometeor size sorting and tornadic potential in simulated supercells. *Mon. Wea. Rev.*, **151**, 1863–1884, https://doi.org/10.1175/MWR-D-22-0228.1.

Marion, G. R., R. J. Trapp, and S. W. Nesbitt, 2019: Using overshooting top area to discriminate potential for large, intense tornadoes. *Geophys. Res. Lett.*, **46**, 12 520–12 526, https://doi.org/10.1029/2019GL084099.

Markowski, P. M., and Y. P. Richardson, 2017: Large sensitivity of near-surface vertical vorticity development to heat sink location in idealized simulations of supercell-like storms. *J. Atmos. Sci.*, **74**, 1095–1104, https://doi.org/10.1175/JAS-D-16-0372.1.

——, J. M. Straka, and E. N. Rasmussen, 2002: Direct surface thermodynamic observations within the rear-flank downdrafts

of nontornadic and tornadic supercells. *Mon. Wea. Rev.*, **130**, 1692–1721, https://doi.org/10.1175/1520-0493(2002)130<1692:DSTOWT>2.0.CO;2.

Martinaitis, S. M., 2017: Radar observations of tornado-warned convection associated with tropical cyclones over Florida. *Wea. Forecasting*, **32**, 165–186, https://doi.org/10.1175/WAF-D-16-0105.1.

May, R. M., S. C. Arms, P. T. Marsh, E. Bruning, and J. R. Leeman, 2017: MetPy: A Python package for meteorological data. Unidata, accessed 17 November 2023, https://doi.org/10.5065/D6WW7G29.

McCaul, E. W., Jr., 1991: Buoyancy and shear characteristics of hurricane-tornado environments. *Mon. Wea. Rev.*, **119**, 1954–1978, https://doi.org/10.1175/1520-0493(1991)119<1954:BASCOH>2.0.CO;2.

——, and M. L. Weisman, 1996: Simulations of shallow supercell storms in landfalling hurricane environments. *Mon. Wea. Rev.*, **124**, 408–429, https://doi.org/10.1175/1520-0493(1996)124<0408:SOSSSI>2.0.CO;2.

——, D. E. Buechler, S. J. Goodman, and M. Cammarta, 2004: Doppler radar and lightning network observations of a severe outbreak of tropical cyclone tornadoes. *Mon. Wea. Rev.*, **132**, 1747–1763, https://doi.org/10.1175/1520-0493(2004)132<1747:DRALNO>2.0.CO;2.

Molinari, J., and D. Vollaro, 2008: Extreme helicity and intense convective towers in Hurricane Bonnie. *Mon. Wea. Rev.*, **136**, 4355–4372, https://doi.org/10.1175/2008MWR2423.1.

——, and ——, 2010: Distribution of helicity, CAPE, and shear in tropical cyclones. *J. Atmos. Sci.*, **67**, 274–284, https://doi.org/10.1175/2009JAS3090.1.

Mulholland, J. P., J. M. Peters, and H. Morrison, 2021: How does LCL height influence deep convective updraft width? *Geophys. Res. Lett.*, **48**, e2021GL093316, https://doi.org/10.1029/2021GL093316.

Nowotarski, C. J., J. Spotts, R. Edwards, S. Overpeck, and G. R. Woodall, 2021: Tornadoes in Hurricane Harvey. *Wea. Forecasting*, **36**, 1589–1609, https://doi.org/10.1175/WAF-D-20-0196.1.

NWS, 2012: Hurricane Irene, August 21–30, 2011. NOAA/NWS Service Assessment, 129 pp., https://www.nws.noaa.gov/om/assessments/pdfs/Irene2012.pdf.

Palmer, R. D., and Coauthors, 2011: Observations of the 10 May 2010 tornado outbreak using OU-PRIME: Potential for new science with high-resolution polarimetric radar. *Bull. Amer. Meteor. Soc.*, **92**, 871–891, https://doi.org/10.1175/2011BAMS3125.1.

Peters, J. M., C. J. Nowotarski, and H. Morrison, 2019: The role of vertical wind shear in modulating maximum supercell updraft velocities. *J. Atmos. Sci.*, **76**, 3169–3189, https://doi.org/10.1175/JAS-D-19-0096.1.

——, ——, J. P. Mulholland, and R. L. Thompson, 2020: The influences of effective inflow layer streamwise vorticity and storm-relative flow on supercell updraft properties. *J. Atmos. Sci.*, **77**, 3033–3057, https://doi.org/10.1175/JAS-D-19-0355.1.

Picca, J., and A. Ryzhkov, 2012: A dual-wavelength polarimetric analysis of the 16 May 2010 Oklahoma City extreme hailstorm. *Mon. Wea. Rev.*, **140**, 1385–1403, https://doi.org/10.1175/MWR-D-11-00112.1.

Potvin, C. K., K. L. Elmore, and S. J. Weiss, 2010: Assessing the impacts of proximity sounding criteria on the climatology of significant tornado environments. *Wea. Forecasting*, **25**, 921–930, https://doi.org/10.1175/2010WAF2222368.1.

Pruppacher, H. R., and R. L. Pitter, 1971: A semi-empirical determination of the shape of cloud and rain drops. *J. Atmos. Sci.*, **28**, 86–94, https://doi.org/10.1175/1520-0469(1971)028<0086:ASEDOT>2.0.CO;2.

Richardson, L. M., W. D. Zittel, R. R. Lee, V. M. Melnikov, R. L. Ice, and J. G. Cunningham, 2017: Bragg scatter detection by the WSR-88D. Part II: Assessment of Z_{DR} bias estimation. *J. Atmos. Oceanic Technol.*, **34**, 479–493, https://doi.org/10.1175/JTECH-D-16-0031.1.

Romine, G. S., D. W. Burgess, and R. B. Wilhelmson, 2008: A dual-polarization-radar-based assessment of the 8 May 2003 Oklahoma City area tornadic supercell. *Mon. Wea. Rev.*, **136**, 2849–2870, https://doi.org/10.1175/2008MWR2330.1.

Ryzhkov, A. V., S. E. Giangrande, V. M. Melnikov, and T. J. Schuur, 2005: Calibration issues of dual-polarization radar measurements. *J. Atmos. Oceanic Technol.*, **22**, 1138–1155, https://doi.org/10.1175/JTECH1772.1.

Scharfenberg, K. A., and Coauthors, 2005: The Joint Polarization Experiment: Polarimetric radar in forecasting and warning decision making. *Wea. Forecasting*, **20**, 775–788, https://doi.org/10.1175/WAF881.1.

Schneider, D., and S. Sharp, 2007: Radar signatures of tropical cyclone tornadoes in central North Carolina. *Wea. Forecasting*, **22**, 278–286, https://doi.org/10.1175/WAF992.1.

Schultz, L. A., and D. J. Cecil, 2009: Tropical cyclone tornadoes, 1950–2007. *Mon. Wea. Rev.*, **137**, 3471–3484, https://doi.org/10.1175/2009MWR2896.1.

Seliga, T. A., and V. N. Bringi, 1976: Potential use of radar differential reflectivity measurements at orthogonal polarizations for measuring precipitation. *J. Appl. Meteor.*, **15**, 69–76, https://doi.org/10.1175/1520-0450(1976)015<0069:PUORDR>2.0.CO;2.

Sessa, M. F., and R. J. Trapp, 2020: Observed relationship between tornado intensity and pretornadic mesocyclone characteristics. *Wea. Forecasting*, **35**, 1243–1261, https://doi.org/10.1175/WAF-D-19-0099.1.

Snyder, J. C., A. V. Ryzhkov, M. R. Kumjian, A. P. Khain, and J. Picca, 2015: A Z_{DR} column detection algorithm to examine convective storm updrafts. *Wea. Forecasting*, **30**, 1819–1844, https://doi.org/10.1175/WAF-D-15-0068.1.

Spratt, S. M., and A. J. Nash, 1995: Central Florida WSR-88D observations and NWSO operations during Tropical Cyclones Alberto, Beryl and Gordon (1994). Preprints, *17th Conf. on Hurricanes and Tropical Meteorology*, Miami, FL, Amer. Meteor. Soc., 298–300.

——, D. W. Sharp, P. Welsh, A. Sandrik, F. Alsheimer, and C. Paxton, 1997: A WSR-88D assessment of tropical cyclone outer rainband tornadoes. *Wea. Forecasting*, **12**, 479–501, https://doi.org/10.1175/1520-0434(1997)012<0479:AWAOTC>2.0.CO;2.

Stumpf, G. J., A. Witt, E. D. Mitchell, P. L. Spencer, J. T. Johnson, M. D. Eilts, K. W. Thomas, and D. W. Burgess, 1998: The National Severe Storms Laboratory mesocyclone detection algorithm for the WSR-88D. *Wea. Forecasting*, **13**, 304–326, https://doi.org/10.1175/1520-0434(1998)013<0304:TNSSLM>2.0.CO;2.

Thompson, E. J., S. A. Rutledge, B. Dolan, M. Thurai, and V. Chandrasekar, 2018: Dual polarization radar rainfall estimation over tropical oceans. *J. Appl. Meteor. Climatol.*, **57**, 755–775, https://doi.org/10.1175/JAMC-D-17-0160.1.

Thompson, R. L., R. Edwards, J. A. Hart, K. L. Elmore, and P. Markowski, 2003: Close proximity soundings within supercell environments obtained from the Rapid Update Cycle. *Wea.*

Forecasting, **18**, 1243–1261, https://doi.org/10.1175/1520-0434(2003)018<1243:CPSWSE>2.0.CO;2.

Tokay, A., P. G. Bashor, E. Habib, and T. Kasparis, 2008: Raindrop size distribution measurements in tropical cyclones. *Mon. Wea. Rev.*, **136**, 1669–1685, https://doi.org/10.1175/2007MWR2122.1.

Trapp, R. J., D. M. Wheatley, N. T. Atkins, R. W. Przybylinski, and R. Wolf, 2006: Buyer beware: Some words of caution on the use of severe wind reports in postevent assessment and research. *Wea. Forecasting*, **21**, 408–415, https://doi.org/10.1175/WAF925.1.

——, G. R. Marion, and S. W. Nesbitt, 2017: The regulation of tornado intensity by updraft width. *J. Atmos. Sci.*, **74**, 4199–4211, https://doi.org/10.1175/JAS-D-16-0331.1.

——, ——, and ——, 2018: Reply to "Comments on 'The regulation of tornado intensity by updraft width'". *J. Atmos. Sci.*, **75**, 4057–4061, https://doi.org/10.1175/JAS-D-18-0276.1.

Turnage, T. J., 2014: An evaluation of normalized rotation vorticity couplets to assess tornadic mesocyclone potential. *27th Conf. of Severe Local Storms*, Madison, WI, Amer. Meteor. Soc., 136, https://ams.confex.com/ams/27SLS/webprogram/Paper254857.html.

Van Den Broeke, M. S., 2016: Polarimetric variability of classic supercell storms as a function of environment. *J. Appl. Meteor. Climatol.*, **55**, 1907–1925, https://doi.org/10.1175/JAMC-D-15-0346.1.

——, 2017: Polarimetric radar metrics related to tornado life cycles and intensity in supercell storms. *Mon. Wea. Rev.*, **145**, 3671–3686, https://doi.org/10.1175/MWR-D-16-0453.1.

——, 2020: A preliminary polarimetric radar comparison of pretornadic and nontornadic supercell storms. *Mon. Wea. Rev.*, **148**, 1567–1584, https://doi.org/10.1175/MWR-D-19-0296.1.

——, 2021: Polarimetric radar characteristics of tornadogenesis failure in supercell thunderstorms. *Atmosphere*, **12**, 581, https://doi.org/10.3390/atmos12050581.

——, J. M. Straka, and E. N. Rasmussen, 2008: Polarimetric radar observations at low levels during tornado life cycles in a small sample of classic Southern Plains supercells. *J. Appl. Meteor. Climatol.*, **47**, 1232–1247, https://doi.org/10.1175/2007JAMC1714.1.

Warren, R. A., H. Richter, H. A. Ramsay, S. T. Siems, and M. J. Manton, 2017: Impact of variations in upper-level shear on simulated supercells. *Mon. Wea. Rev.*, **145**, 2659–2681, https://doi.org/10.1175/MWR-D-16-0412.1.

Wienhoff, Z. B., H. B. Bluestein, L. J. Wicker, J. C. Snyder, A. Shapiro, C. K. Potvin, J. B. Houser, and D. W. Reif, 2018: Applications of a spatially variable advection correction technique for temporal correction of dual-Doppler analyses of tornadic supercells. *Mon. Wea. Rev.*, **146**, 2949–2971, https://doi.org/10.1175/MWR-D-17-0360.1.

Wilson, M. B., and M. S. Van Den Broeke, 2021: An automated Python algorithm to quantify Z_{DR} arc and K_{DP}–Z_{DR} separation signatures in supercells. *J. Atmos. Oceanic Technol.*, **38**, 371–386, https://doi.org/10.1175/JTECH-D-20-0056.1.

——, and ——, 2022: Using the Supercell Polarimetric Observation Research Kit (SPORK) to examine a large sample of pretornadic and nontornadic supercells. *Electron. J. Severe Storms Meteor.*, **17** (2), https://doi.org/10.55599/ejssm.v17i2.85.